J. Fluid Mech. (1993), *vol.* 255, *pp.* 503–539

Direct numerical simulation of turbulent flow over riblets

By HAECHEON CHOI, PARVIZ MOIN AND JOHN KIM

Center for Turbulence Research, Stanford University, Stanford, CA 94305 *and* NASA Ames Research Center, Moffett Field, CA 94035, USA

(Received 28 July 1992 and in revised form 28 January 1993)

Direct numerical simulations of turbulent flows over riblet-mounted surfaces are performed to educe the mechanism of drag reduction by riblets. The computed drag on the riblet surfaces is in good agreement with the existing experimental data. The mean-velocity profiles show upward and downward shifts in the log–law for drag-decreasing and drag-increasing cases, respectively. Turbulence statistics above the riblets are computed and compared with those above a flat plate. Differences in the mean-velocity profile and turbulence quantities are found to be limited to the inner region of the boundary layer. Velocity and vorticity fluctuations as well as the Reynolds shear stresses above the riblets are reduced in drag-reducing configurations. Quadrant analysis indicates that riblets mitigate the positive Reynolds-shear-stress-producing events in drag-reducing configurations. From examination of the instantaneous flow fields, a drag reduction mechanism by riblets is proposed: riblets with small spacings reduce viscous drag by restricting the location of the streamwise vortices above the wetted surface such that only a limited area of the riblets is exposed to the downwash of high-speed fluid that the vortices induce.

1. Introduction

Organized structures have been observed in turbulent flows over the past three decades and are known to play an important role in turbulent transport (Cantwell 1981; Robinson 1991). The awareness of the existence of deterministic structures has led to substantial research in turbulence control. Skin-friction reduction in turbulent flow has been investigated by several different passive means, such as riblets, large-eddy breakup devices, polymer additions, and compliant walls (see Bushnell & McGinley 1989; Coustols & Savill 1992). Among those tested to date, surface-mounted longitudinal grooves have been most successful in reducing the net drag of turbulent boundary layers in spite of a substantial increase in the wetted surface area.

Walsh & Weinstein (1978) and Walsh (1980, 1982, 1983) showed that V-groove riblet surfaces can produce consistent net drag reductions (as large as 8%) provided that the height and spacing of the grooves are less than $25\,\nu/u_\tau$, where ν and u_τ denote the kinematic viscosity and the wall-shear velocity, respectively. The effects of riblets on turbulent boundary layers have been investigated by several other researchers: Hooshmand *et al.* (1983), Gallagher & Thomas (1984), Bacher & Smith (1985), Sawyer & Winter (1987), Wallace & Balint (1987), Wilkinson & Lazos (1987), Bechert & Bartenwerfer (1989), Choi (1989), and Vukoslavčević, Wallace & Balint (1992), to name a few. Nitschke (1984), Liu *et al.* (1990), and Nakao (1991) studied the effects of riblets in turbulent pipe flows. Their results were in good agreement with previous investigations of turbulent boundary-layer flows over riblets.

The mechanisms by which riblets reduce drag, however, remain poorly understood. Two possible mechanisms have been proposed. The first is that the skin-friction reduction in the riblet valleys might be sufficient to overcome the skin-friction increase near riblet tips. The second is that riblet tips actually reduce momentum transport by impeding the cross-flow motion. Walsh & Weinstein (1978) and Walsh (1980) designed riblet surfaces to confine the turbulent 'wall bursts' to their initial birth regions. Gallagher & Thomas (1984) suggested from a flow visualization study that the observed drag reductions result less from a direct interaction of riblets with the turbulence than from the low velocities in the bottoms of the grooves. Bacher & Smith (1985) observed by a flow visualization that, below $y^+ = yu_\tau/\nu = 15$, the lateral movement of the streaks above a riblet surface is substantially less than the lateral movement observed above a flat surface. They suggested that the secondary vortices generated at the riblet peaks weaken the well known near-wall streamwise vortices and inhibit the spanwise concentration of low-speed fluid into streak formations. Wallace & Balint (1987) reviewed the existing experimental data and proposed that riblets shield the surface from much of the turbulent momentum transport, resulting in smaller velocity gradients on the bounding surface. Robinson (1988) studied the effects of riblets on turbulence in a supersonic boundary layer. He hypothesized that riblets reduce skin friction by impeding the cross-stream flow necessary to replace the near-wall fluid that is ejected during turbulence production events. Bechert & Bartenwerfer (1989) introduced a so-called 'protrusion height' for different types of riblets and related it to the ability of riblets to impede the cross-flow. Choi (1989) indicated that the restriction of spanwise movement of the longitudinal vortices is a prime mechanism for turbulent drag reduction.

Choi, Moin & Kim (1991) studied the effect of riblets in fully developed laminar channel flows in order to investigate whether the skin-friction reduction in the riblet valley is sufficient to compensate for the skin-friction increase in the region of the tip. They showed that drag reduction is not obtained in the laminar channel flow even though the wall-shear rate on most of the riblet surface was smaller than that of the corresponding flat channel flow.

Effects of riblets on turbulence statistics have been reported by several authors. These include an upward shift in the log–law velocity profile due to an increase of viscous sublayer thickness, a displaced virtual origin of the wall, a reduction of turbulence intensities and Reynolds shear stress, a decrease of momentum thickness, an increase of the mean streak spacing, little change in the skewness and flatness factors of the streamwise fluctuating velocity, and limited changes of the mean velocity and turbulence quantities in the inner regions of the boundary layer.

The reported changes in turbulence statistics are not conclusive, however, and no clear picture of the drag reduction mechanism set up by riblets has emerged. The difficulty in measurement of velocity fields near riblets and the modest change in skin friction and turbulence statistics have hampered efforts to understand the mechanics of drag reduction.

In recent years, numerical simulations of turbulent flows have become an important tool for studying the basic physics of turbulence (Rogallo & Moin 1984). Kim, Moin & Moser (1987) performed a direct numerical simulation of a turbulent channel flow. A large variety of turbulence statistics were computed and compared with the existing experimental data at comparable Reynolds numbers. Jiménez & Moin (1991) performed direct numerical simulations of unsteady channel flow at low to moderate Reynolds numbers on computational boxes chosen small enough so that the flow consists of a doubly periodic array of identical structures. The goal of their work was

to isolate the basic flow unit, to study its morphology and dynamics, and to evaluate its contribution to turbulence in fully developed channels. They showed that the near-wall turbulence statistics and presumable flow mechanisms in the minimal channel are in good agreement with the 'natural' channel.

The objective of this work is to perform direct numerical simulations of turbulent flows over riblets, to analyse the resulting flow database, and to educe the mechanism of drag reduction by riblets. Such an understanding can potentially lead to the design of riblet configurations that give even higher drag reduction. In this paper we describe the results of these simulations and our observations on the drag reduction mechanism. The computed results are compared with available experimental data. The computational domain and grid spacing are described in §2, followed in §3 by the numerical method developed for complex geometries. Section 4 describes the drag variation due to riblets and the virtual origin of the wall. Turbulence statistics are reported in §5. Modified turbulent structures and mechanisms of drag reduction by riblets are presented in §6, followed by a brief summary in §7.

In this paper, x_1, x_2, and x_3 denote the streamwise (x), wall-normal (y), and spanwise (z) directions, respectively. The velocity notations u_1, u_2, and u_3 in the x-, y-, and z-directions are used interchangeably with u, v, and w. The subscript w indicates the value at the wall, and the superscript + indicates a non-dimensional quantity scaled by the wall variables; for example, $y^+ = yu_\tau/\nu$, where $u_\tau = (\tau_w/\rho)^{\frac{1}{2}}$ is the wall-shear velocity.

2. Computational domain and grid spacing

The flow geometry and coordinate system are shown in figure 1. The upper wall is a flat plate, whereas the lower wall is a plate with riblets. Fully developed turbulent flow over riblets is homogeneous in the streamwise (x_1) direction, and periodic boundary conditions are used in the streamwise (x_1) and spanwise (x_3) directions. The non-slip condition is applied at both walls. The simulation imposes a constant instantaneous volume flux in the streamwise direction,

$$Q = \int_{A_c} u_1 \, \mathrm{d}A = \tfrac{2}{3} A_c U_l,$$

where $A_c = L_{x_2} L_{x_3}$ is the cross-sectional area, and U_l is the centreline velocity of a laminar parabolic profile with the same volume flux. The computation is carried out for a Reynolds number of 4200 based on the laminar centreline velocity U_l and the channel half-width δ ($= \frac{1}{2} L_{x_2}$); i.e.

$$Re = \frac{3Q}{4\nu L_{x_3}} = \frac{U_l \delta}{\nu}.$$

This Reynolds number corresponds to a Reynolds number, Re_τ, of about 180 based on the wall-shear velocity of the flat plate, u_{τ_f}. For the Reynolds number considered here, the computational box is chosen to be about one-and-half times larger than a *minimal flow unit* of Jiménez & Moin (1991) in the spanwise direction in order to allow for the possible increase of the streak spacings above the riblets; the streamwise and spanwise computational periods, L_{x_1} and L_{x_3}, are $\pi\delta$ and $0.289\pi\delta$, respectively (roughly 570 and 160 wall units).

A uniform mesh with spacing $\Delta x_1^+ \approx 35$ is used in the streamwise direction. This streamwise spacing is rather coarse; however, for comparison the calculations of flows over both riblets and a flat surface were carried out with the same resolution. A direct numerical simulation of turbulent channel flow was performed to investigate the

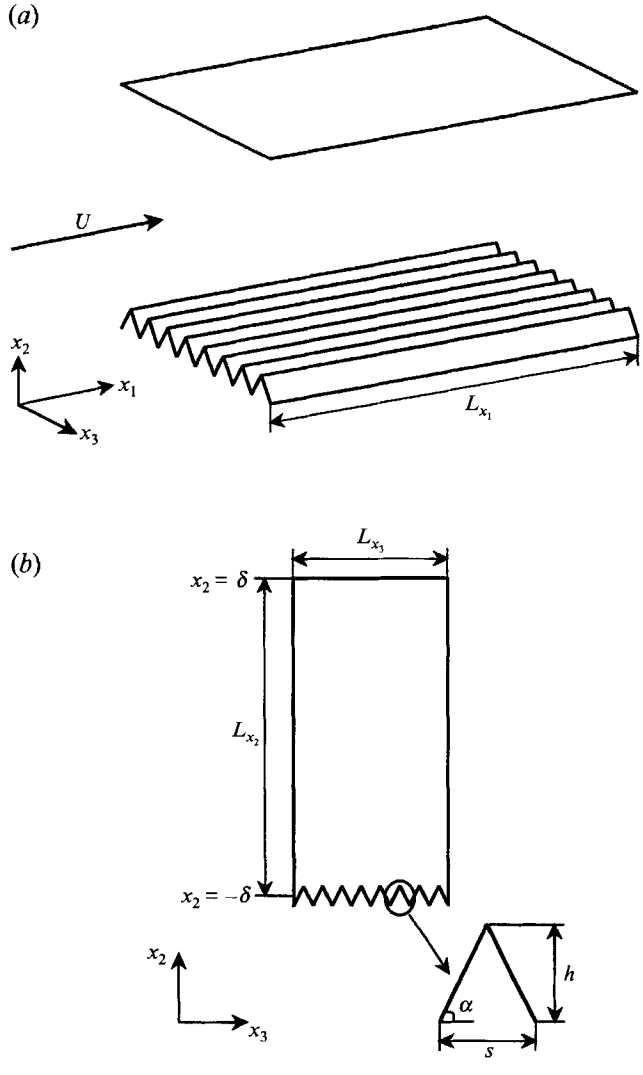

FIGURE 1. (*a*) Three-dimensional view of computational domain; (*b*) cross-sectional view of riblet configuration.

sensitivity of turbulence statistics to the computational resolution (Choi, Moin & Kim 1992). This study showed that doubling the grid points in both the streamwise and spanwise directions (from $16 \times 129 \times 32$ to $32 \times 129 \times 64$) changed the maximum turbulence intensities and the Reynolds shear stress by less than 2%. Although strictly we cannot claim streamwise grid independence of the results, the fact that both the plane wall and the wall with riblets are conducted with the same resolution should be adequate for comparison purposes. The grid resolution in the spanwise direction, Δx_3^+, is finer than that of Kim *et al.* (1987). The resolution in the wall-normal direction is about the same as theirs. A non-uniform mesh of 129 points with a hyperbolic tangent distribution is used in the wall-normal direction. The first mesh point away from the flat wall is at $x_2^+ \approx 0.15$, and the maximum spacing at the centreline of the channel is 7 wall units. A non-uniform orthogonal mesh developed by Bechert & Bartenwerfer (1989) is used in the wall-normal and spanwise directions; the non-uniform mesh is

Case	s/δ	s^+	h^+	α (deg.)	$N_{x_1} \times N_{x_2} \times N_{x_3}$	Δx_3^+
A	0.2270	40	20.0	45	$16 \times 129 \times 128$	1.28
B	0.2270	40	34.6	60	$16 \times 129 \times 128$	1.28
C	0.1135	20	10.0	45	$16 \times 129 \times 256$	0.64
D	0.1135	20	17.3	60	$16 \times 129 \times 256$	0.64

TABLE 1. Parameters for the simulations of turbulent flows over riblets. N_{x_i} is the number of grid points in the x_i direction.

distributed using a conformal mapping such that the shear *force* of each numerical cell on the riblet is constant when the mean-flow distribution is a uniform Couette flow very near the riblet. An extensive spanwise grid refinement study was performed to ensure adequate resolution. Thirty-two grid points on each riblet surface are necessary to resolve the high-shear rates near the riblet tips. Doubling the number of mesh points in the spanwise direction changes the drag on the riblet surface by less than 1%. Insufficient grid resolution in the spanwise direction results in an underestimation of the skin friction as observed by Launder & Li (1989). The spacing between adjacent grid points far above the riblet surface, Δx_3^+, is approximately 1 wall unit in the present calculation which is much finer than that in Kim *et al.* (1987) (see table 1). An example of the computational mesh near riblets in a cross-flow plane is shown in figure 2.

We have tested four riblet configurations: riblet spacings of 20 and 40 wall units and ridge angles α of 45° and 60°. A detailed description of the parametric study is shown in table 1. The results from cases A–D near the riblets are compared to those near the flat wall.

3. Numerical methods

The governing equations for an incompressible flow can be written in the following form:

$$\frac{\partial u_i}{\partial t} + \frac{\partial}{\partial x_j} u_i u_j = -\frac{\partial p}{\partial x_i} + \frac{1}{Re} \frac{\partial}{\partial x_j} \frac{\partial}{\partial x_j} u_i, \tag{1}$$

$$\frac{\partial u_i}{\partial x_i} = 0, \tag{2}$$

where x_i are Cartesian coordinates, and u_i are the corresponding velocity components. All variables are non-dimensionalized by the channel half-width δ and the laminar centreline velocity U_l. In these units, the value of the laminar spanwise vorticity magnitude at the flat channel wall is $|\omega_z| = 2$. Re denotes the Reynolds number, defined as $Re = U_l \delta / \nu$.

Equations (1) and (2) are written in a conservative form in generalized coordinates as

$$\frac{\partial q^i}{\partial t} + N^i(\boldsymbol{q}) = -G^i(p) + L_1^i(\boldsymbol{q}) + L_2^i(\boldsymbol{q}), \tag{3}$$

$$\mathrm{D}^i q^i = \frac{\partial q^1}{\partial \eta^1} + \frac{1}{J}\left(\frac{\partial q^2}{\partial \eta^2} + \frac{\partial q^3}{\partial \eta^3}\right) = 0, \tag{4}$$

where $\boldsymbol{q} = (q^1, q^2, q^3)$, N^i is the convection term, $G^i(p)$ is the pressure gradient term, L_1^i and L_2^i are the diffusion terms without and with cross-derivatives, respectively, and D^i is the divergence operator. Here, we introduce generalized coordinates for the wall-normal and spanwise directions (i.e. $(x_2, x_3) \rightarrow (\eta^2, \eta^3)$), and use a Cartesian coordinate

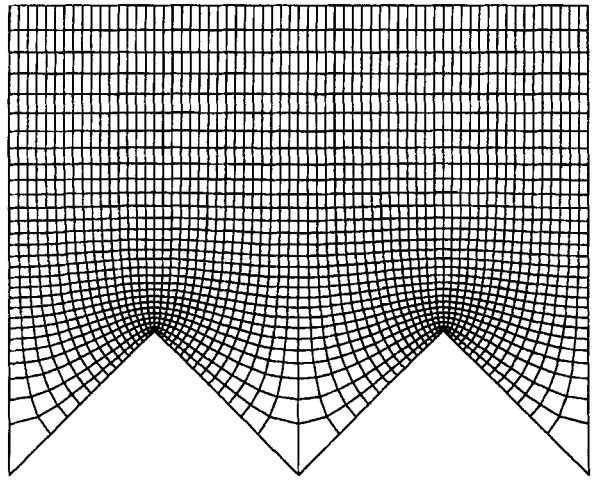

FIGURE 2. Computational mesh near riblets in the case of $s^+ \approx 20$ and $\alpha = 45°$. A non-uniform mesh of 129 points with hyperbolic tangent distribution is used in the wall-normal direction, and thirty-two grid points are used on each riblet surface.

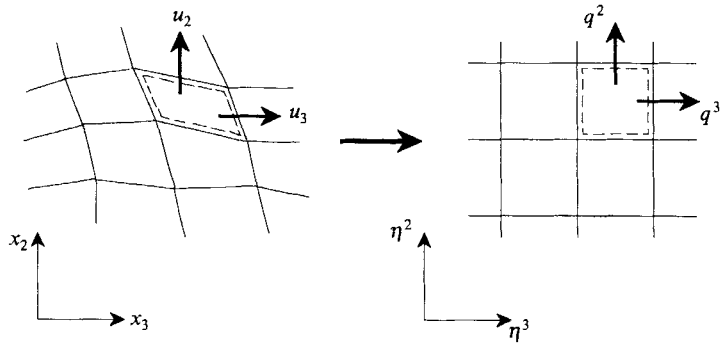

FIGURE 3. Coordinate transformation.

for the streamwise direction ($\eta^1 = x_1$). The q^i are volume fluxes across the faces of the cells, which are equivalent to using the contravariant velocity components on a staggered grid multiplied by the Jacobian of the coordinate transformation, J (figure 3). Using this choice, the discretized mass conservation can be easily satisfied (Rosenfeld, Kwak & Vinokur 1991). The terms in (3) are (the summation convention applies)

for $i = 1$,

$$\left.\begin{aligned} N^1 &= \frac{\partial}{\partial \eta^1} q^1 q^1 + \frac{1}{J}\frac{\partial}{\partial \eta^j} q^j q^1, \\ G^1(p) &= \frac{\partial p}{\partial \eta^1}, \\ L_1^1 &= \frac{1}{Re}\left(\frac{\partial}{\partial \eta^1}\frac{\partial}{\partial \eta^1} q^1 + \frac{1}{J}\frac{\partial}{\partial \eta^k}\alpha^{kj}\frac{\partial}{\partial \eta^j} q^1\right); \quad j = k, \\ L_2^1 &= \frac{1}{Re}\frac{1}{J}\frac{\partial}{\partial \eta^k}\alpha^{kj}\frac{\partial}{\partial \eta^j} q^1; \quad j \neq k, \end{aligned}\right\} \tag{5}$$

for $i = 2, 3$,

$$\left.\begin{aligned} N^i &= \frac{\partial}{\partial \eta^1} q^1 q^i + \frac{1}{J}\gamma^i_m \frac{\partial}{\partial \eta^j}\frac{1}{J} c^m_k\, q^k q^j, \\ G^i(p) &= \alpha^{ij}\frac{\partial p}{\partial \eta^j}, \\ L^i_1 &= \frac{1}{Re}\left(\frac{\partial}{\partial \eta^1}\frac{\partial}{\partial \eta^1} q^i + \frac{1}{J}\gamma^i_m \frac{\partial}{\partial \eta^k}\alpha^{kj}\frac{\partial}{\partial \eta^j}\frac{1}{J} c^m_l\, q^l\right); \quad j = k, \\ L^i_2 &= \frac{1}{Re}\frac{1}{J}\gamma^i_m \frac{\partial}{\partial \eta^k}\alpha^{kj}\frac{\partial}{\partial \eta^j}\frac{1}{J} c^m_l\, q^l; \quad j \neq k, \end{aligned}\right\} \tag{6}$$

where

$$q^1 = u_1, \quad q^j = \gamma^j_k u_k, \quad c^j_k = \partial x_j/\partial \eta^k, \quad \gamma^j_k = J(c^k_j)^{-1}, \quad \alpha^{jk} = J(c^m_j\, c^m_k)^{-1},$$
$$J = (\|c^m_j\, c^m_k\|)^{\frac{1}{2}}, \quad \text{and} \quad j, k, l, m = 2, 3.$$

The integration method used to solve (3) and (4) is based on a fully implicit, fractional step method (Choi *et al.* 1992); all terms in (3) including cross-derivative diffusion terms are advanced with the Crank–Nicolson method in time, and are resolved with the second-order central-difference scheme in space. A Newton method is used to solve the discretized nonlinear equations. The suitability of a second-order central-difference scheme for direct simulation of turbulent channel flow is discussed in Choi *et al.* (1992).

Rapid variation of skin friction near the riblet tips requires dense grid clustering in their vicinity; this would restrict the computational time step for numerical stability if an explicit or (as in the usual practice in direct simulation) a semi-implicit method were used. In a separate study, we found the largest computational time step (in wall units) that accurately predicted turbulence statistics in a turbulent plane channel flow at $Re = 4200$ (Choi *et al.* 1992). For cases A–D (table 1), we have used this same computational time step, $\Delta t U_l/\delta = 0.05$ ($\Delta t^+ \approx 0.4$). About seven Newton iterations were needed to solve the discretized nonlinear momentum equations. The CPU time required for cases C and D was about 60 Cray-YMP seconds per time step. For all cases, the computations were carried out for 500 non-dimensional time units (tU_l/δ), which corresponds to about 4000 viscous time units ($tu^2_{\tau_f}/\nu$). Ten thousand time steps were required for each case. The conventional semi-implicit method would have required about a five-fold increase in the required CPU time.

4. Drag measurement, mean-velocity profile, and the virtual origin

For each case (A–D), random disturbances were initially imposed upon the laminar mean velocity profile. Starting from these initial velocity fields, the governing equations were integrated forward in time until the numerical solutions reached statistically steady states. These equilibrium states were identified by a quasi-periodic behaviour of the wall-shear stresses. Once the velocity field reached the statistically steady state, the equations were integrated further in time to obtain the time average of the various statistical quantities. The total averaging time was $500\,\delta/U_l$ ($\approx 4000\nu/u^2_{\tau_f}$) for all results reported here. In this section, an overbar indicates average over x, t, and the

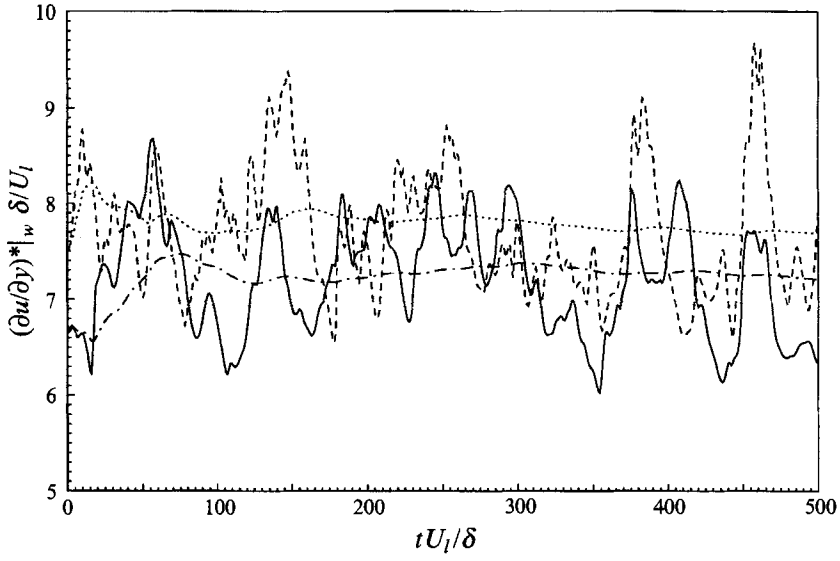

FIGURE 4. Time history of wall-shear rates at both flat and riblet walls for $s^+ \approx 20$ and $\alpha = 60°$. Instantaneous plane-averaged wall-shear rate: —, at the riblet wall, $(\partial u/\partial y)_r^*$; – – –, at the flat plate, $(\partial u/\partial y)_f^*$. Plane- and time-averaged wall-shear rates: – · –, at the riblet wall; · · · · · · · · ·, at the flat plate. $(\partial u/\partial y)|_w \delta/U_l = 2$ corresponds to fully developed laminar plane channel flow.

same spanwise locations over different riblets, and a prime indicates perturbation from this average.

4.1. *Drag measurement*

The average skin-friction drag is obtained as the integral of the product of the wall-shear stress and the differential wetted area. Note that the wetted area of a plate with riblets is sec(α) times wider than that of a flat plate, where α is the ridge angle of the riblet (figure 1*b*). The drag variation due to the presence of riblets is calculated by comparing the skin friction of the flat plate (upper wall) and the plate with riblets (lower wall). This comparison relies upon the observation that turbulent flow near one side of channel does not affect the skin friction at the other. It was shown in Jiménez & Moin (1991) that the correlation coefficient between the shear histories at the two walls of a symmetric channel is always small, $|corr| \leqslant 0.15$, indicating that the intermittent behaviour acts independently at each wall.

The instantaneous plane-averaged drag of the flat surface, D_f, and of the riblet surface, D_r, are computed with

$$\left.\begin{aligned} D_f &= \mu \int_{A_f} \frac{\partial u}{\partial n} \mathrm{d}A_f = \mu \left(\frac{\partial u}{\partial y}\right)_f^* A_f, \\ D_r &= \mu \int_{A_r} \frac{\partial u}{\partial n} \mathrm{d}A_r = \mu \left(\frac{\partial u}{\partial y}\right)_r^* A_f, \end{aligned}\right\} \tag{7}$$

where n is the coordinate normal to the surface, and A_r and A_f denote the wetted areas of the riblet and flat surfaces, respectively; $A_r = L_{x_1} \times N_r\, s \sec(\alpha)$ and $A_f = A_r \cos(\alpha) = L_{x_1} \times L_{x_3}$. Here, N_r is the number of riblets in the computational domain; $N_r = 4$ and 8 for the cases $s^+ \approx 40$ and 20, respectively.

Case	s^+	h^+	α (deg.)	Present study	Walsh (1982)
A	40	20.0	45	+2%	+3%
B	40	34.6	60	+12%	+11%*
C	20	10.0	45	−5%	−2%
D	20	17.3	60	−6%	−4%*

TABLE 2. Drag variation for each riblet configuration. In the last two columns + and − denote the drag increase and decrease, respectively, and * denotes data obtained from the case $s^+ = h^+$.

Figure 4 shows the time history of the average wall-shear rates, $(\partial u/\partial y)_f^*$ and $(\partial u/\partial y)_\tau^*$, for the case $s^+ \approx 20$ and $\alpha = 60°$. Stochastic and intermittent behaviour of the wall-shear rates is clearly discernible. This intermittency is due to the limited size of the computational box in the (x, z)-plane and the correspondingly small statistical sample of near-wall events. Clearly, further averaging in time is required. The histories of plane- and time-averaged wall-shear rates, i.e. $1/t\int_0^t(\partial u/\partial y)_f^*(\tau)\,\mathrm{d}\tau$ and $1/t\int_0^t(\partial u/\partial y)_\tau^*(\tau)\,\mathrm{d}\tau$, are also shown in figure 4. The drag reduction by the riblets is clearly evident.

Table 2 shows the drag increase or decrease for each riblet configuration studied. Also given are the experimental results of Walsh (1982) for similar riblet geometries. The error bounds in Walsh's drag measurements were reported to be about $\pm 1\%$. Error bounds for statistical sampling errors for the present drag measurements were obtained by comparing the wall-shear rates of the *two flat walls* in a plane channel simulation; the values of averaged wall-shear rates should be identical, with sufficient time averaging. After averaging over 500 non-dimensional time units (tU_l/δ), the remaining fluctuation was about $\pm 2\%$. Thus, the data in table 2 show a reasonable agreement in the drag variation between the present study and the experimental data.

4.2. *Mean streamwise-velocity profile and origin of the wall*

Figure 5 shows the variation of the mean velocity in the transverse plane. No apparent spanwise variation of the mean velocity is found above $y/\delta \approx -0.9$ in the case $s^+ \approx 20$ or above $y/\delta \approx -0.8$ in the case $s^+ \approx 40$. Note that the midpoint of the riblet valley and tip corresponds to $y/\delta = -1$ (figure 1*b*). The spanwise variation of the mean velocity occurs only very near the riblets where, at a given y, the mean velocity above the riblet valley is larger than that above the riblet tip. These observations have also been reported in experimental (Hooshmand *et al.* 1983; Benhalilou *et al.* 1991; Vukoslavčević *et al.* 1992) and analytical (Bechert & Bartenwerfer 1989) studies.

The lack of spanwise variation of the mean velocity above a certain y-location suggests the use of a *virtual origin*. The virtual origin for riblets is defined as the location y_o of an *imaginary flat surface* which has the *same drag* as the riblet-mounted surface and matches the riblet velocity profile above the viscous sublayer. For the case of the smooth wall, the virtual origin is located at the surface.

Definitions of the virtual origin and the friction velocity at that position are useful for comparison of the results with the flat-plate data. There have been four methods used to evaluate the virtual origin of the riblet wall: (i) using a modified Clauser's method (Hooshmand *et al.* 1983), (ii) using a measured linear velocity profile inside the viscous sublayer (Hooshmand *et al.* 1983), (iii) using a velocity defect profile above the inner region (Choi 1989), and (iv) using a conformal mapping, assuming that a linear velocity region exists inside the viscous sublayer (Bechert & Bartenwerfer 1989; Luchini, Manzo & Pozzi 1991).

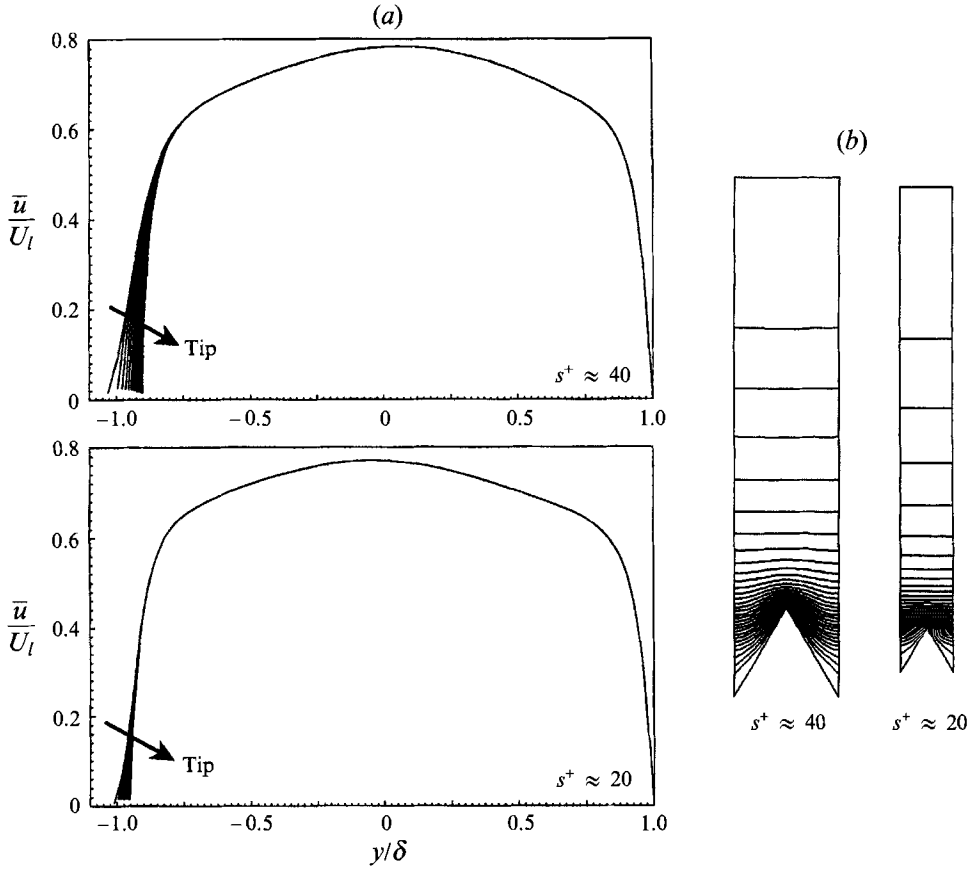

FIGURE 5. Mean velocity profiles for $\alpha = 60°$. (*a*) One-dimensional view with different spanwise locations; (*b*) contours of the mean velocity in the (y, z)-plane. The contour levels normalized by U_l range from 0 to 0.75 by increments of 0.025. The plot domain extends from the riblet surface to the centreline of the channel.

Figure 6 shows the wall-shear rate and the contribution to the drag as a function of the spanwise position along the riblet for all configurations tested. The wall-shear rate at the riblet surface is defined as

$$\frac{\partial \overline{u}}{\partial n}(z) = \frac{1}{T}\frac{1}{L_x}\int_0^T \int_0^{L_x} \frac{\partial u}{\partial n}(x, z, t)\,\mathrm{d}x\,\mathrm{d}t.$$

The wall-shear rate over most of the riblet surface is smaller than that of the corresponding plane turbulent channel flow. In cases with $\alpha = 45°$, the wall-shear rates near the tip and valley regions are nearly identical regardless of riblet spacing (it has been shown by Moffatt & Duffy 1980 and Choi *et al.* 1991 that, when the convection terms of (1) are negligible, local similarity solutions and asymptotic behaviour exist near corners and the velocity distributions very near corners (tip or valley) are governed mostly by the angle of the corner). However, near the middle of riblets, the wall-shear rate of riblets with $s^+ \approx 40$ is noticeably higher than that with $s^+ \approx 20$. Riblets with $\alpha = 60°$ show the same trend. This difference in the wall-shear rate near the middle of the riblet determines the net performance of riblets of a given spacing. Note that the integration of the curves in figure 6(*b*) gives the drag on the riblets.

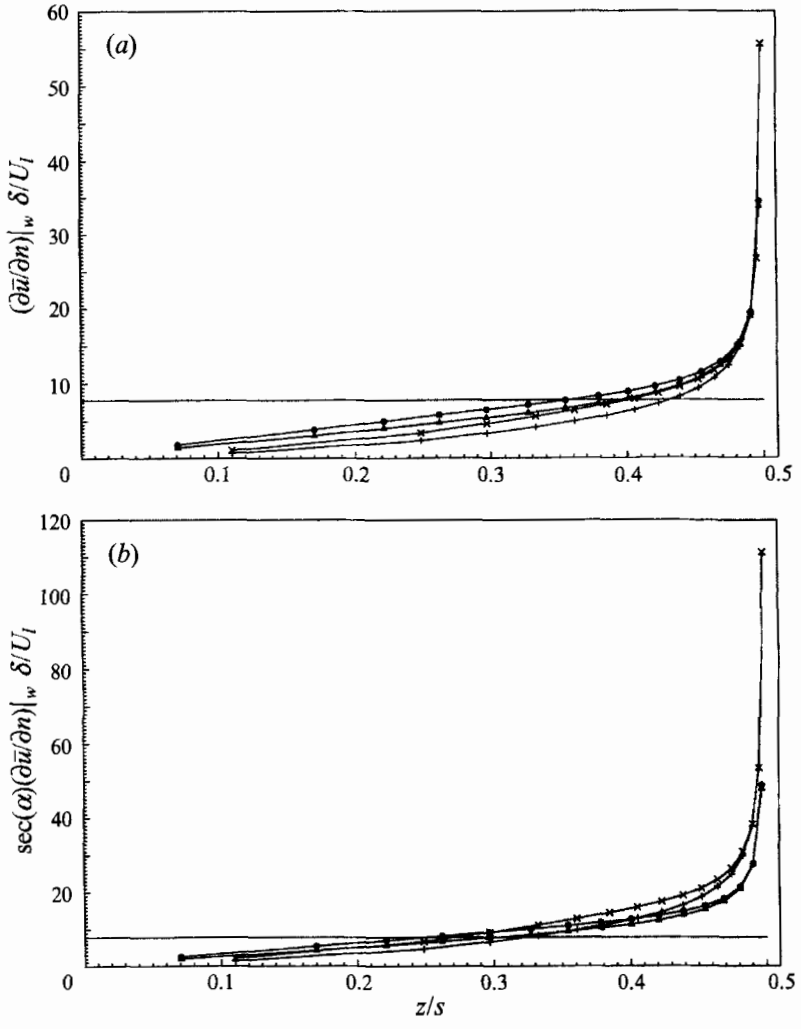

FIGURE 6. (*a*) Wall-shear rates and (*b*) contribution to the drag at several spanwise positions on riblet surfaces: ●, $s^+ \approx 40$ and $\alpha = 45°$; ▲, $s^+ \approx 20$ and $\alpha = 45°$; ×, $s^+ \approx 40$ and $\alpha = 60°$; +, $s^+ \approx 20$ and $\alpha = 60°$. $z/s = 0$ and 0.5 correspond to the valley and tip of the riblet, respectively. Solid line denotes the value of the wall-shear rate on the flat-plate side. $(\partial\bar{u}/\partial n)|_w\,\delta/U_l = 2$ corresponds to fully developed laminar plane channel flow.

Time- and plane-averaged drag of the riblet surface, $\bar{D}_r$, is obtained by

$$\bar{D}_r = \frac{1}{T}\int_0^T D_r\,\mathrm{d}t = \mu\left(\frac{\partial\bar{u}}{\partial y}\right)_r^* A_f, \tag{8}$$

where D_r is defined in (7). The wall-shear velocity $u_{\tau_r}^*$ at the virtual origin is defined by

$$u_{\tau_r}^* = \left(\nu\left(\frac{\partial\bar{u}}{\partial y}\right)_r^*\right)^{\frac{1}{2}}. \tag{9}$$

The wall-shear velocities defined by (9) for each riblet configuration are shown in table 3. Before exploring the four different methods described previously for obtaining the

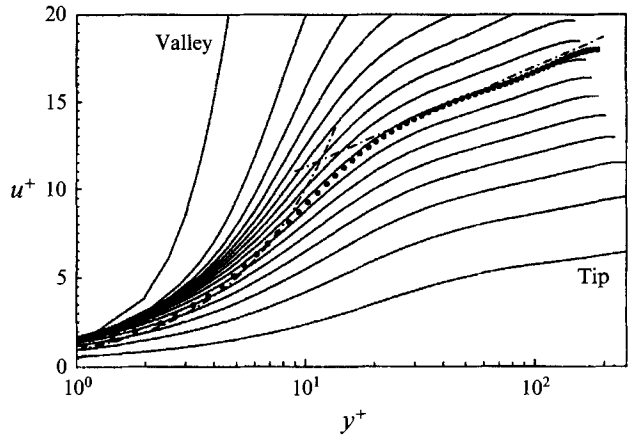

FIGURE 7. Mean-velocity profiles normalized by the local wall-shear velocity, $u_{\tau_r}(z)$ for $s^+ \approx 20$ and $\alpha = 60°$: —, mean velocity over the riblet at different spanwise locations; ●, mean velocity over the flat plate; –·–, laws of the wall ($u^+ = y^+$ and $u^+ = 2.5 \ln y^+ + 5.5$). $u_{\tau_r}(z) = (\nu(\partial\bar{u}/\partial n)|_w)^{\frac{1}{2}}$. The wall-shear rates are shown in figure 6.

Case	$u^*_{\tau_r}/U_l$	$\beta^\dagger$	$\beta^\ddagger$	y^+_{tip}	$F^\dagger$	$F^\ddagger$
A	0.0435	0.11	0.12 ± 0.02	5.4	-0.1	-0.5
B	0.0456	0.26	0.30 ± 0.02	5.8	-1.0	-1.0
C	0.0418	0.11	0.19 ± 0.05	1.2	$+0.9$	$+1.0$
D	0.0414	0.26	0.33 ± 0.05	2.0	$+0.9$	$+1.0$

TABLE 3. Wall-shear velocity and location of the virtual origin for each riblet configuration. For the flat plate, $u_{\tau_f}/U_l = 0.0430$ and $U_c/u_{\tau_f} = 18.1$, where U_c is the centreline velocity. $\beta^\dagger$ is from Bechert & Bartenwerfer (1989); $y_o/\delta = -1 + \beta s/\delta$, and $\beta^\ddagger$ is from equation (10); $y_o/\delta = -1 + \beta s/\delta$. Error bounds for $\beta^\ddagger$ are obtained noting a 10% variation of the location y^+_m. Note that $y_o/\delta = -1$ corresponds to the midpoint between the riblet tip and valley. $y^+_{tip} = (y_{tip} - y_o)u^*_{\tau_r}/\nu$; y_o is obtained from equation (10). $F^\dagger$ is from Gaudet (1987) (see equation (12)) and $F^\ddagger$ from equation (12) (y_o is obtained from equation (10)).

virtual origin, consider plots of the mean-velocity profiles, normalized by the local wall-shear velocities $u_{\tau_r} = (\nu \partial\bar{u}/\partial n)^{\frac{1}{2}}$, at various points along the perimeter of the riblet surface (figure 7). Significant downward shifts in the log–law are obtained near the riblet tip, whereas significant upward shifts are obtained near the riblet valley. Note that this plot is normalized by the *local* wall-shear velocity, not by $u^*_{\tau_r}$.

In most experimental studies, the location of the virtual origin is taken to be the riblet tip, valley, or the midpoint between the tip and valley. Figure 8 shows the variation of the mean-velocity profile with different choices of the virtual origin for cases with $\alpha = 60°$. Here, the wall-shear velocity is chosen to be $u^*_{\tau_r}$ (equation (9)). This plot does not contain the velocity inside the viscous sublayer because of the spanwise variation of the mean velocity there. The slope of the log–law above the riblets is little changed as compared with the flat-plate profile. In the case $s^+ \approx 20$, the intercept of the log–law with $u^+ = y^+$ is farther away from the wall regardless of the location of the virtual origin (when the *local* wall-shear velocity was used, both upward and downward shifts in the log–law were obtained (figure 7)). This upward shift in the log–law has previously been observed in drag-reduced flows such as large-eddy breakup devices (Bandyopadhyay 1986; Nguyen, Savill & Westphal 1987), riblets

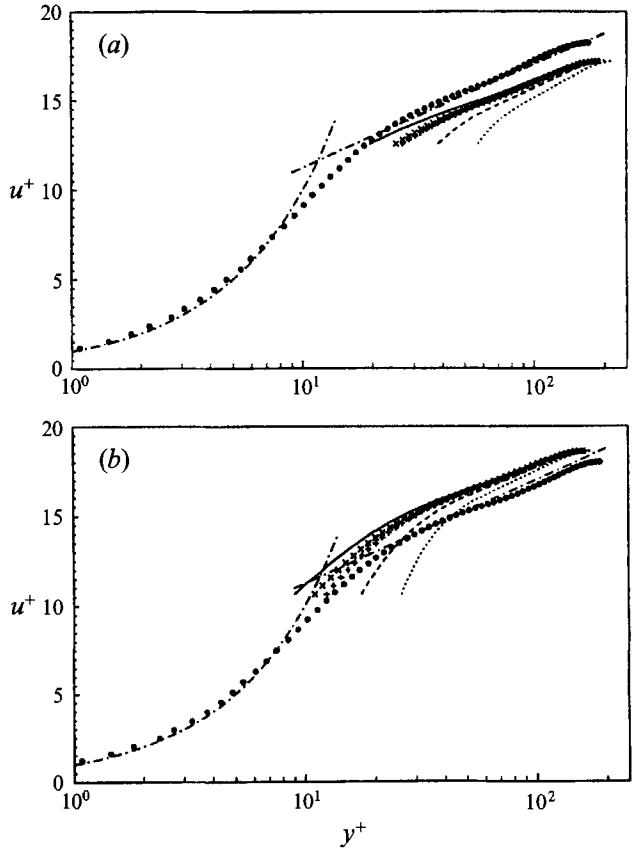

FIGURE 8. Variation of mean-velocity profiles normalized by the wall-shear rates, u_τ^* (equation (9)), with the location of the virtual origin for $\alpha = 60°$: (*a*) $s^+ \approx 40$; (*b*) $s^+ \approx 20$. The virtual origin is located: — at the riblet tip; – – –, at the midpoint between tip and valley, · · · · · · · · ·, at the riblet valley; +, at the location from Bechert & Bartenwerfer (1989); ×, at the location from equation (10). –·–, Laws of the wall; ●, mean velocity over the flat wall.

(Hooshmand *et al.* 1983; Choi 1989), and polymers (Lumley 1973; Virk 1975), and it may be considered the result of the increase of the viscous sublayer thickness. On the other hand, in the case $s^+ \approx 40$, the location of the intercept is decreased, indicating a decrease of the viscous sublayer thickness. Cases with $\alpha = 45°$ show the same trend (Choi *et al.* 1992).

The four methods of evaluating the virtual origin of the wall discussed earlier are based on the existence of either a linear velocity region or a logarithmic region near the surface. The logarithmic region for the present calculation is quite narrow (figure 8), so the application of methods (i) and (iii) will not give an accurate estimation of the location of the virtual origin. Method (ii) is also not useful since the location of the virtual origin depends on the baseline of the mean velocity (see figure 3 in Hooshmand *et al.* 1983). Bechert & Bartenwerfer (1989) determined the location of the virtual origin of the wall, y_o, using a conformal mapping, assuming that a linear velocity region exists inside the viscous sublayer; using their method, for $\alpha = 45°$, $y_o/\delta = -1 + 0.11 s/\delta$, and for $\alpha = 60°$, $y_o/\delta = -1 + 0.26 s/\delta$. The mean-velocity profile based on this virtual origin is shown in figure 8. Again, an upward shift in the log–law is evident in the case $s^+ \approx 20$. However, the weak point of the method of Bechert & Bartenwerfer (1989) is

that it cannot be used for flows for which the drag is increased because in such cases the riblet surface is not completely immersed in the viscous sublayer.

It should be mentioned that all the existing methods of evaluating the virtual origin are based on changes in the mean streamwise velocity rather than changes in turbulence structure. Since an upward shift in the log–law is closely related to the balance between turbulent energy production and viscous dissipation (Lumley 1973), measurement of changes of turbulent structure above the wall may be another criterion to determine the virtual origin. The maximum turbulent kinetic energy production on the flat-plate side occurs at $y^+ \approx 13$, as does the maximum intensity of the streamwise velocity fluctuations. One may therefore define the virtual origin from

$$y_m^+ \approx 13 = \frac{(y_m - y_o)\, u_{\tau_r}^*}{\nu},$$

where y_m and y_o are the locations of the maximum turbulent kinetic energy production (or the maximum streamwise velocity fluctuation intensity) and the virtual origin, respectively. Therefore, the location of the virtual origin is

$$y_o = y_m - \frac{13\nu}{u_{\tau_r}^*}. \tag{10}$$

The location of the virtual origin y_o may be obtained from the profile of the streamwise velocity fluctuation intensity (figure 11) for each riblet configuration, and is tabulated in table 3, together with results by Bechert & Bartenwerfer (1989). It can be clearly seen that, as the ridge angle increases, the virtual origin moves closer to the riblet tip. The location of the riblet tip, $y_{tip}^+ = (y_{tip} - y_o)\, u_{\tau_r}^*/\nu$, is tabulated in table 3, where y_o is obtained from (10). The riblet surfaces with $s^+ \approx 20$ are completely immersed in the viscous sublayer.

There is a rough agreement between the present method and that of Bechert & Bartenwerfer: the distance between the two virtual origins is $\Delta y_o^+ = \Delta y_o\, u_{\tau_r}^*/\nu = (\beta^\ddagger - \beta^\dagger) s^+$ which is about 1.6 wall units for the present riblet configurations. $\beta^\ddagger$ and $\beta^\dagger$ are tabulated in table 3. Note that the present method requires the profile of the streamwise velocity fluctuations to determine the virtual origin location, while Bechert & Bartenwerfer's method only requires the riblet ridge angle. Clearly, the advantage of Bechert & Bartenwerfer's method is that it does not require any measurements of flow variables. However, their virtual origin location is fixed with a given ridge angle regardless of flow conditions, such as Reynolds number, riblet spacing, etc. Since variations in such parameters lead to different drag values, its definition implies that the virtual origin should be a function of the flow parameters.

The mean-velocity profiles based on these virtual origins for cases with $\alpha = 60°$ are shown in figure 8. The mean-velocity profiles by the method of Bechert & Bartenwerfer (1989) and equation (10) are nearly identical in the log–law region. Near the wall region ($y^+ < 20$), however, the mean-velocity profiles differ a little due to the slight difference in virtual origins. The upward and downward shifts in the log–law are clearly seen for drag-decreasing and drag-increasing cases, respectively. Cases with $\alpha = 45°$ show the same trend (Choi *et al.* 1992).

The velocity profile in the wall region of a turbulent boundary layer is described by

$$\frac{\bar{u}}{u_{\tau_f}} = \frac{1}{\kappa} \ln \frac{u_{\tau_f} y}{\nu} + B, \tag{11}$$

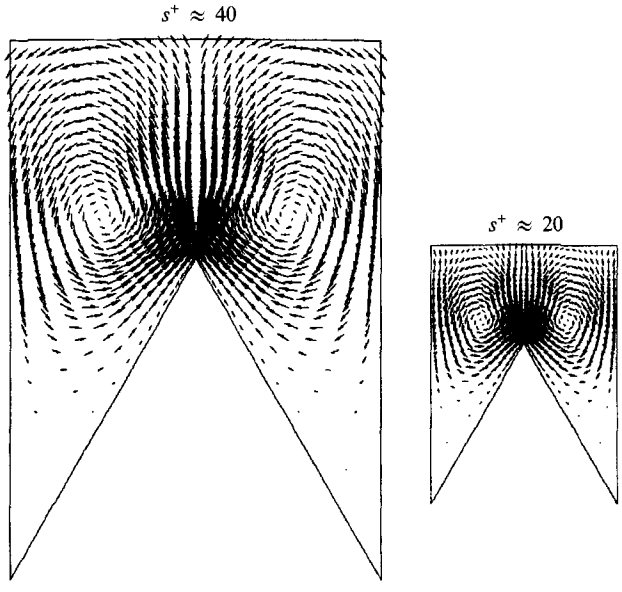

FIGURE 9. Mean secondary velocity vectors $(\bar{v}, \bar{w})$ in the transverse plane for $\alpha = 60°$. The secondary flow vectors for $s^+ \approx 20$ are enlarged by a factor of two as compared to $s^+ \approx 40$.

where $\kappa = 0.4$ and $B = 5.5$ (for low-Reynolds-number flows). For rough surfaces, the velocity profile has been described by (11) with the addition of a function F of the surface roughness parameter (Nikuradse 1933; Schlichting 1936). This modified representation of the mean-velocity profile has been used to model the mean flow over riblets by Sawyer & Winter (1987), Gaudet (1987) and Tani (1988):

$$\frac{\bar{u}}{u_{\tau_r}^*} = \frac{1}{\kappa} \ln \frac{u_{\tau_r}^*(y - y_o)}{\nu} + B + F. \tag{12}$$

Since $u_{\tau_r}^*$ and y_o are given in table 3, the constant F for each riblet configuration may be obtained and is listed in table 3. It is clear from table 3 that F is positive for drag-reducing cases and is negative for drag-increasing cases. Values of F obtained in this study are compared with those by Gaudet (1987) in table 3; except for case A, good agreement is found between the two results.

4.3. *Mean secondary motion near the riblets*

Mean secondary velocity vectors $(\bar{v}, \bar{w})$ near the riblets are shown in figure 9. The secondary flow convects momentum from the central region to the riblet valley along the corner bisector, which results in comparatively large streamwise velocities in the upper region of the riblet valley (figure 5*b*) and then transports momentum away from the riblet valley to the riblet tip along the riblet surface. This phenomenon is quite similar to that occurring in a fully developed turbulent pipe flow with non-circular cross-section (Nikuradse 1930). It is interesting to note that secondary flow cannot be sustained in a fully developed laminar flow in the same geometry (Choi *et al.* 1991). Note that in figure 9 the secondary flow vectors for the case $s^+ \approx 20$ are enlarged by a factor of two as compared to the case $s^+ \approx 40$, indicating that the mean secondary motion in the case $s^+ \approx 40$ is much stronger than that in the case $s^+ \approx 20$. The maximum mean secondary velocities in the cases $s^+ \approx 20$ and $s^+ \approx 40$ are about 0.2%

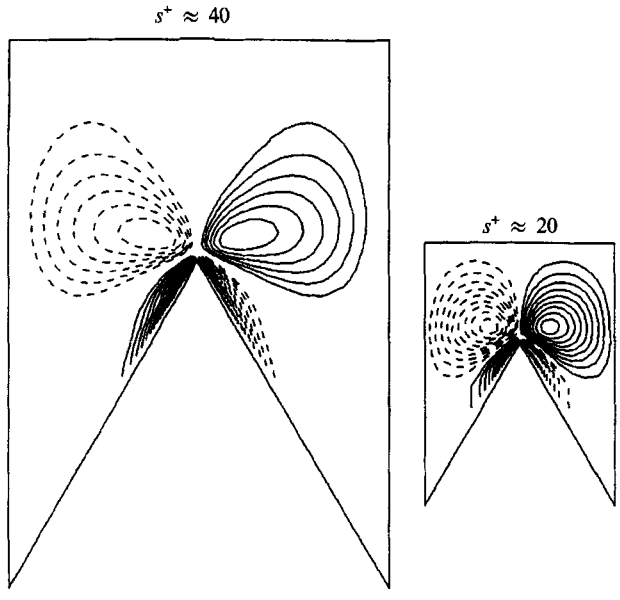

FIGURE 10. Contours of the mean streamwise vorticity, $\bar{\omega}_x \delta/U_c$, in the transverse plane for $\alpha = 60°$. The values of $\bar{\omega}_x \delta/U_c$ at the centres of the vortices are 0.19 ($s^+ \approx 20$) and 0.36 ($s^+ \approx 40$). Increments of the contour levels are 0.02 and 0.04 for $s^+ \approx 20$ and $s^+ \approx 40$, respectively. Negative contours are dashed.

and 0.8% of the mean centreline velocity U_c, respectively. Considering that the maximum wall-normal and spanwise velocity intensities above the riblets are about 5% of U_c (figure 11*b*, *c*), the instantaneous cross-flow fields are much stronger than the mean secondary motion.

Contours of the mean streamwise vorticity are shown in figure 10. Counter-rotating streamwise vortices are clearly seen near the riblets. The spanwise dimension of these vortices is determined by the spacing between the riblets. The values of the mean streamwise vorticity, $\bar{\omega}_x \delta/U_c$, at their centres are 0.19 ($s^+ \approx 20$) and 0.36 ($s^+ \approx 40$), which are much weaker than the instantaneous streamwise vortices frequently observed above the wall (see figures 16*a* and 25). The effect of the mean streamwise vortices on drag-reduction performance by the riblets is unclear.

5. Turbulence statistics

In this section turbulence statistics from the calculations of turbulent flow over the riblets are presented. Flow variables on the side of the channel with the riblets (lower wall) are averaged only in x, t, and the same spanwise locations over different riblets, while those on the side of the flat plate (upper wall) are averaged in x, z and t. Results in both global and wall coordinates are presented. In global coordinates, velocities are normalized by the centreline velocity U_c, and lengths are normalized by the channel half-width δ. When flow variables are plotted in wall coordinates, velocities are normalized by either u_{τ_f} (for the flat plate) or $u^*_{\tau_r}$ (for the plate with riblets), and $y_f^+ = u_{\tau_f} y/\nu$ and $y_r^+ = u^*_{\tau_r}(y-y_o)/\nu$. The virtual origin, y_o, and the wall-shear velocity at that location, $u^*_{\tau_r}$, are obtained from (10) and (9), respectively. The changes in the absolute magnitudes of flow statistics are more evident in global coordinates, whereas wall coordinates are better suited for the structural changes of flow variables. In this

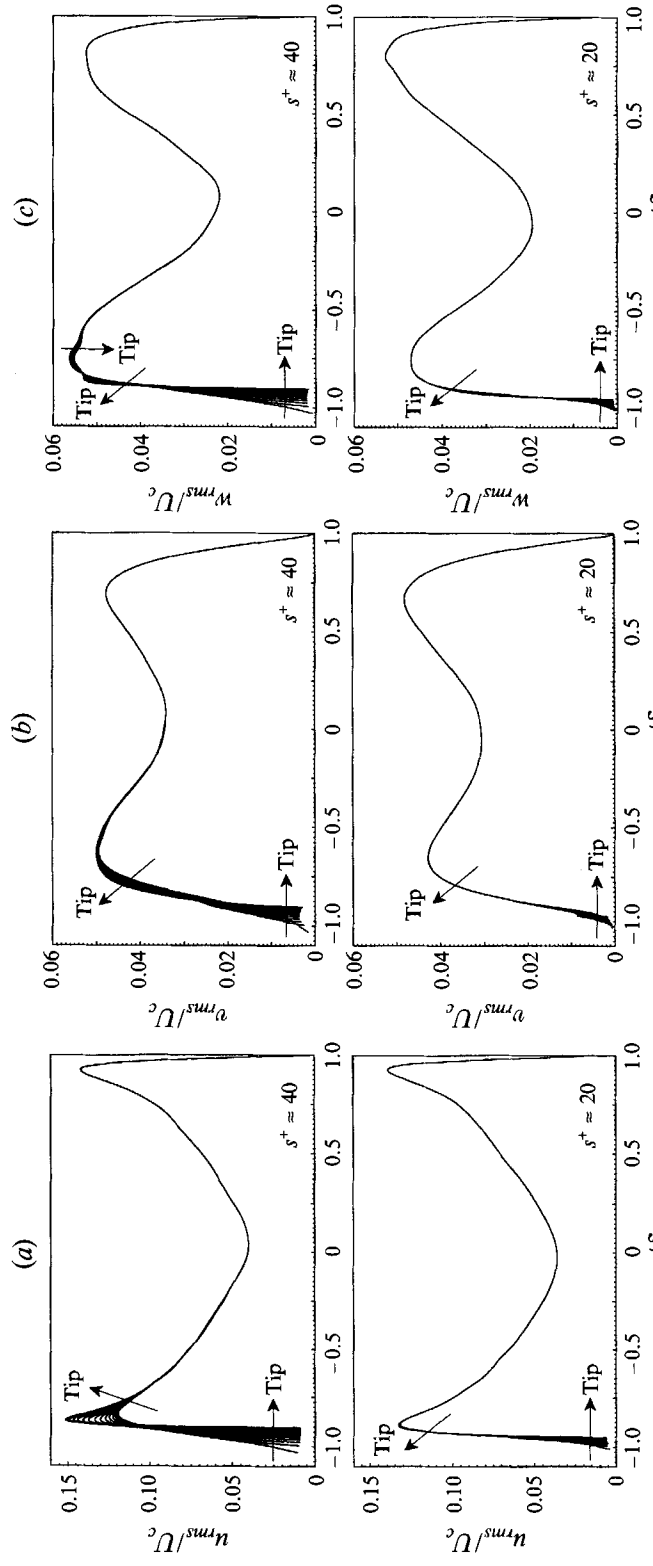

FIGURE 11. Root-mean-square velocity fluctuations normalized by the mean centreline velocity U_c in global coordinates for $\alpha = 60°$. (*a*) Streamwise; (*b*) normal; (*c*) spanwise velocity fluctuations.

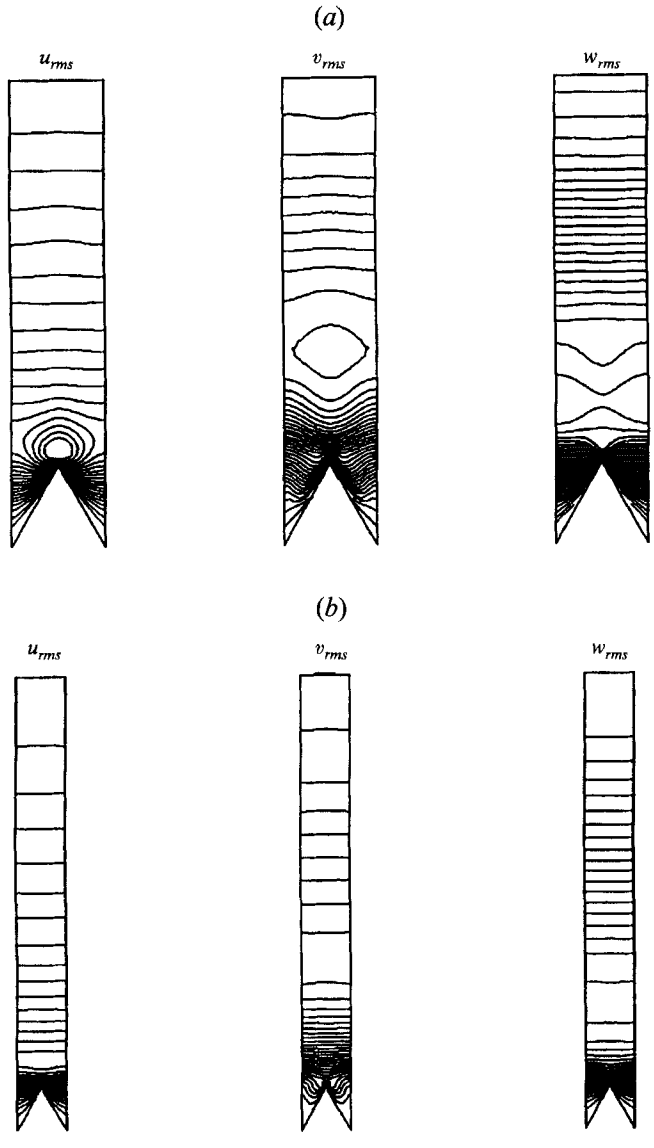

FIGURE 12. Contours of root-mean-square velocity fluctuations in the (y, z)-plane for $\alpha = 60°$: (*a*) $s^+ \approx 40$; (*b*) $s^+ \approx 20$. The increments of contour levels for u_{rms}, v_{rms} and w_{rms} normalized by U_c are 0.0064, 0.0016 and 0.0016, respectively. The plot domain extends from the riblet surface to the centreline of the channel.

section, we present the results of cases with $\alpha = 60°$ ($s^+ \approx 20$ and 40). Riblets with $\alpha = 45°$ showed nearly the same trend (Choi *et al.* 1992).

5.1. *Turbulence intensities*

Turbulence-intensity profiles at various spanwise locations are shown in figure 11, and contours of turbulence intensities in the cross-flow plane are shown in figure 12. Significant variations of the turbulence intensities occur only very near the riblets in the case $s^+ \approx 20$. In the case $s^+ \approx 40$, the effects of the riblets penetrate further into the channel (figure 12), and spanwise variations of the normal and spanwise components

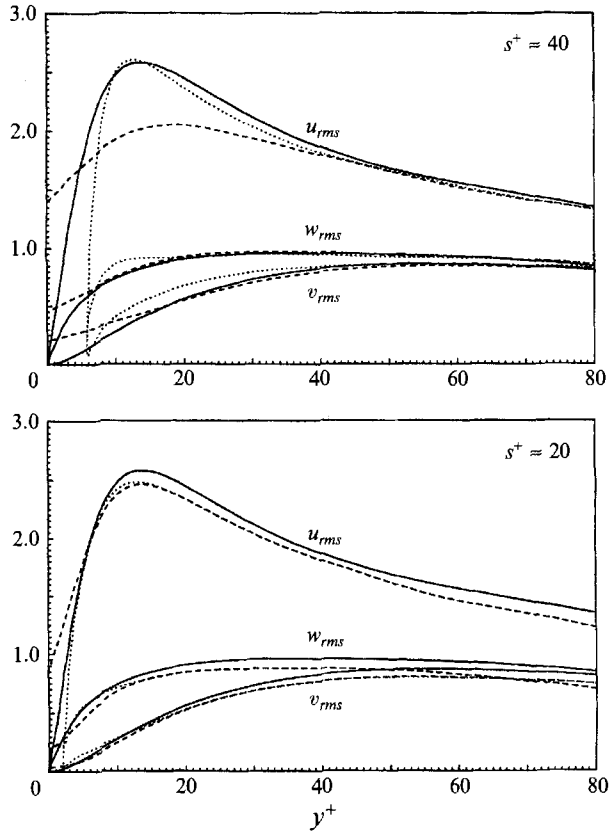

FIGURE 13. Root-mean-square velocity fluctuations normalized by the wall-shear velocity u_τ in wall coordinates for $\alpha = 60°$: ——, above the riblet valley; · · · · · · · · ·, above the riblet tip; —, above the flat plate.

of the turbulence intensity extend even into the region where there is no noticeable spanwise variation of the mean velocity (figure 5) or the streamwise velocity fluctuations (figure 12*a*). This indicates that the cross-flow is more sensitive to the presence of riblets than is the flow in the streamwise direction.

Reduction of all three components of turbulent intensity by the riblets is evident in a drag-reducing configuration ($s^+ \approx 20$) (figure 11). Note that the maximum wall-normal and spanwise root-mean-square velocity fluctuations are reduced by 10%, while only a 5% reduction is obtained in the maximum streamwise root-mean-square velocity fluctuations. Turbulence intensities increase near the riblets in the case $s^+ \approx 40$ (a drag-increasing configuration). The streamwise component of the turbulence intensity is reduced by 15% above the riblet valley and increased by 5% above the riblet tip as compared to the flat-plate case. However, the maximum values of the other two components are increased by 5% across the entire span.

Reductions of the streamwise velocity fluctuations by riblets have been observed in several experiments (Walsh 1980; Hooshmand *et al.* 1983; Nitschke 1984; Johansen & Smith 1986; Choi 1989, Benhalilou *et al.* 1991; Wilkinson & Lazos 1991; Vukoslavčević *et al.* 1992). Bacher & Smith (1985) reported an increase of the streamwise velocity fluctuations, which is clearly contradictory to the present results and other experimental results. There are limited data available for the normal and spanwise velocity

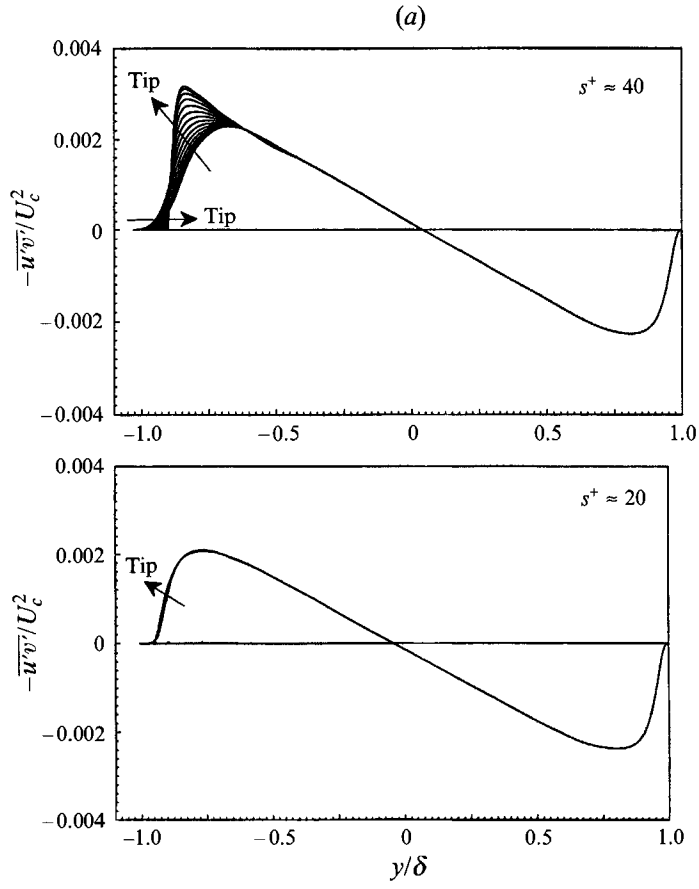

FIGURE 14(*a*). For caption see facing page.

fluctuations. Walsh (1980) found a small reduction in the normal velocity fluctuations. Benhalilou *et al.* (1991) used riblets with $s^+ = 2h^+ \approx 30$ and observed a large reduction of the streamwise and spanwise velocity fluctuations in the vicinity of the riblet valley and a significant increase close to the riblet tip. The behaviour of the streamwise velocity fluctuations in their work is quite similar to the present results for drag-increasing configurations with $s^+ = 1.155h^+ \approx 40$ and $s^+ = 2h^+ \approx 40$ (see § 5.6). As drag was not measured in their study, the increase of the streamwise velocity fluctuations probably resulted from having a drag-increasing configuration. However, reduction of the spanwise velocity fluctuations above the riblet valley, as seen in the results of Benhalilou *et al.* (1991), was not obtained in the present study for drag-increasing configurations. Vukoslavčević *et al.* (1992) measured streamwise velocity fluctuations above riblets with $s^+ = 2h^+ \approx 35$ and found a decrease in magnitude across the entire span. The present study shows that the turbulence intensity above riblets is modified differently depending upon whether the configuration is drag-reducing or drag-increasing. Hence, measurements of turbulence intensities should be accompanied by drag measurements in order to properly correlate these quantities.

Turbulence intensities normalized by either u_{τ_f} (for the flat plate) or $u^*_{\tau_r}$ (for the plate with riblets) are shown in figure 13. The y^+ locations of the peak streamwise velocity fluctuations above both the flat plate and the riblets are nearly identical because of the

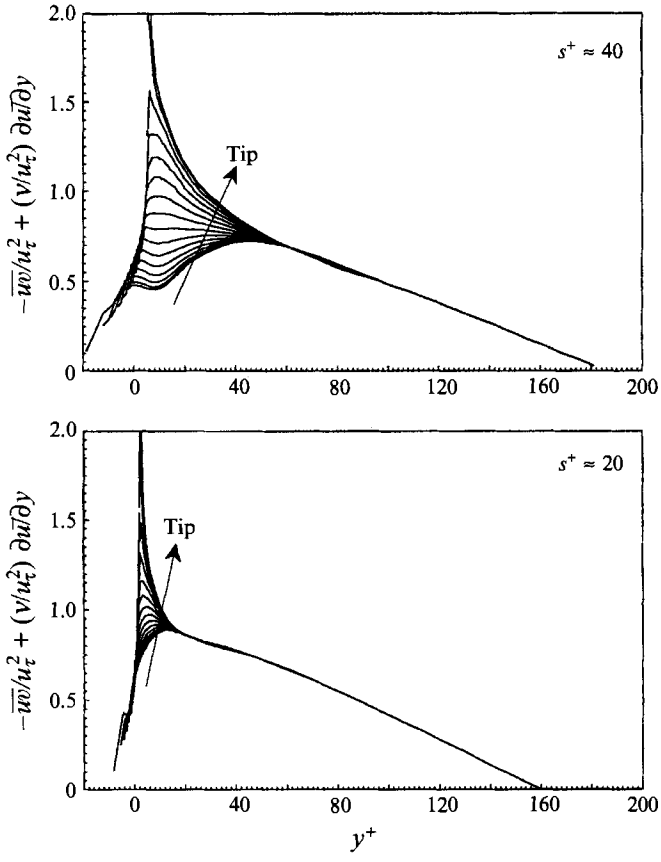

FIGURE 15. Total shear stress normalized by the wall-shear velocity $u_{\tau_r}^*$ in wall coordinates for $\alpha = 60°$.

because the effects of the riblets with $s^+ \approx 40$ penetrate further into the channel (see below). However, in the case $s^+ \approx 20$, there is a good agreement. For the Reynolds number considered here ($Re_\tau = 180$), 40 wall units represents a significant portion of the flow geometry. Therefore, a perturbation to the wall of this magnitude may lead to a significant change in the global characteristics of the flow. On the other hand, turbulence statistics in the case $s^+ \approx 40$ collapse with the flat-plate data for $y^+ > 60$, indicating that even for this seemingly large geometrical perturbation the effects of riblets are confined to the near-wall region.

The total shear stress, $-\overline{uv} + \nu\,\partial\bar{u}/\partial y$, above the riblets is shown in figure 15. Taking the average of the streamwise momentum equation over time and space (x) gives

$$\frac{\partial}{\partial y}\left(-\overline{uv} + \nu\frac{\partial \bar{u}}{\partial y}\right) + \frac{\partial}{\partial z}\left(-\overline{uw} + \nu\frac{\partial \bar{u}}{\partial z}\right) = \frac{1}{\rho}\frac{\partial \bar{p}}{\partial x} = \text{constant}. \tag{13}$$

When the spanwise variations of the mean velocity and shear stresses are negligible compared with their normal variations, the total shear stress becomes linear across the channel. The computed result away from the riblets clearly indicates that this is indeed the case. However, a linear profile is not obtained very near the riblets since the spanwise variations of $-\overline{uw}$ and $\partial\bar{u}/\partial z$ are not negligible (see figures 5*b* and 12). Significant spanwise variation of $-\overline{uw}$ is also reported in Benhalilou *et al.* (1991). This

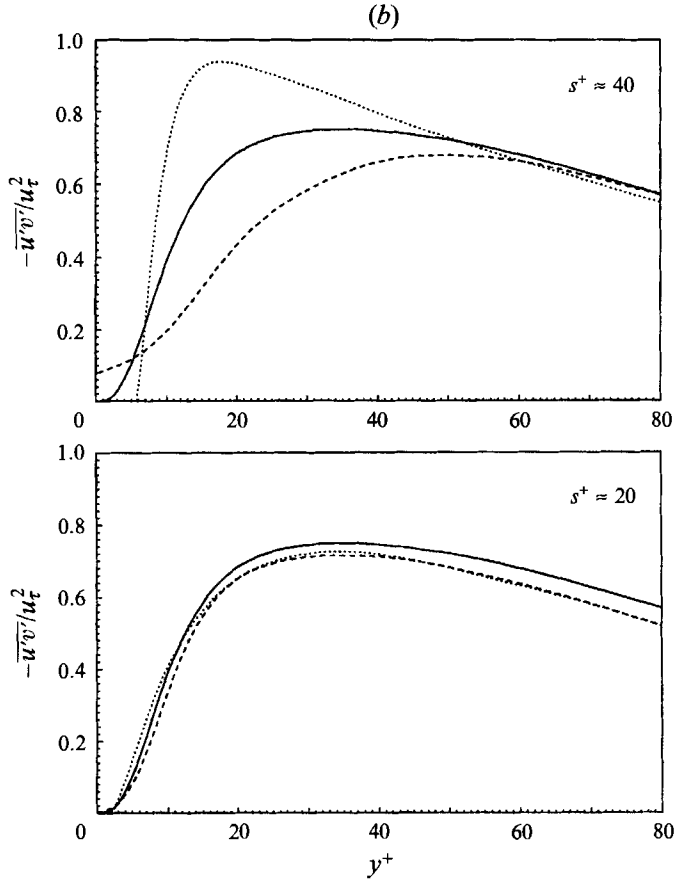

FIGURE 14. Reynolds shear stress for $\alpha = 60°$: (*a*) in global coordinates; (*b*) in wall coordinates, – – –, above the riblet valley; · · · · · · · · ·, above the riblet tip; —, above the flat plate.

particular choice of the virtual-origin location (equation (10)). Profiles of v_{rms} and w_{rms} are also nearly identical. The viscous sublayer is significantly modified by the riblets in all configurations.

5.2. *Reynolds shear stress*

The Reynolds shear stress $-\overline{u'v'}$, normalized by the mean centreline velocity, is shown in figure 14(*a*). In the case $s^+ \approx 20$, the maximum Reynolds shear stress above the riblets is reduced by 12% as compared with that above the flat plate, and there is negligible spanwise variation of the Reynolds shear stress near the riblets. Walsh (1980) reported a maximum reduction of 16% in the Reynolds shear stress above riblets. Pulles, Prasad & Nieuwstadt (1989) showed that the Reynolds shear stress is noticeably reduced through the log-law region for a riblet-mounted surface. In the case $s^+ \approx 40$, however, the maximum Reynolds shear stress above the riblets is significantly increased above the riblet tip and is nearly unaffected above the riblet valley as compared to the flat-plate side. There is also substantial spanwise variation of $-\overline{u'v'}$ near the riblets in this case.

The Reynolds shear stress profiles above the riblets, normalized by the wall-shear velocity $u_{\tau_r}^*$, are shown in figure 14(*b*). Also shown is the Reynolds shear stress above the flat plate. In the case $s^+ \approx 40$, peak locations and magnitudes of the Reynolds shear stress above the riblet tip and valley differ greatly from the flat-plate profile. This is

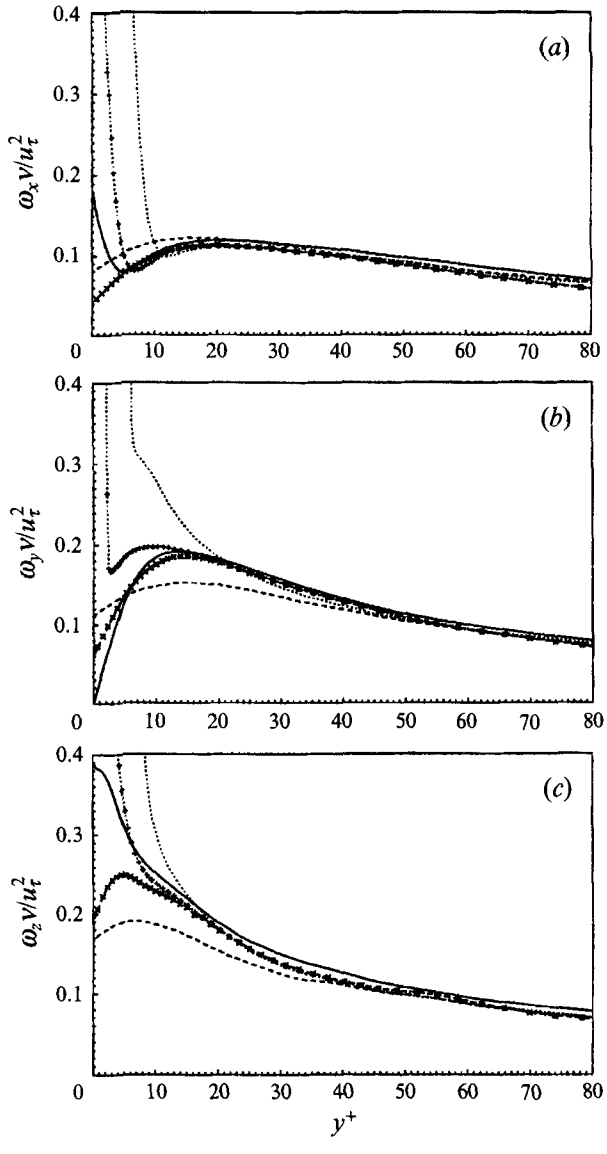

FIGURE 17. Root-mean-square vorticity fluctuations normalized by the wall-shear velocity u_τ in wall coordinates for $\alpha = 60°$. (*a*) Streamwise; (*b*) normal; (*c*) spanwise vorticity fluctuations. —, Above the flat plate. Above the riblet valley: – – –, $s^+ \approx 40$; ×, $s^+ \approx 20$. Above the riblet tip: · · · · · · · ·, $s^+ \approx 40$; +, $s^+ \approx 20$.

deviation from linearity illustrates the zone of influence of the riblets in the channel. For example, in the case $s^+ \approx 20$, the zone of influence is about $y^+ < 20$, while it is about $y^+ < 60$ in the case $s^+ \approx 40$ (figure 15).

5.3. *Vorticity*

There are no known experimental data on vorticity fluctuations above riblets. Root-mean-square vorticity fluctuations normalized by the mean centreline velocity and the channel half-width are shown in figure 16. All three vorticity fluctuation components show maximum values at the riblet tip. Significant spanwise variations of the vorticity

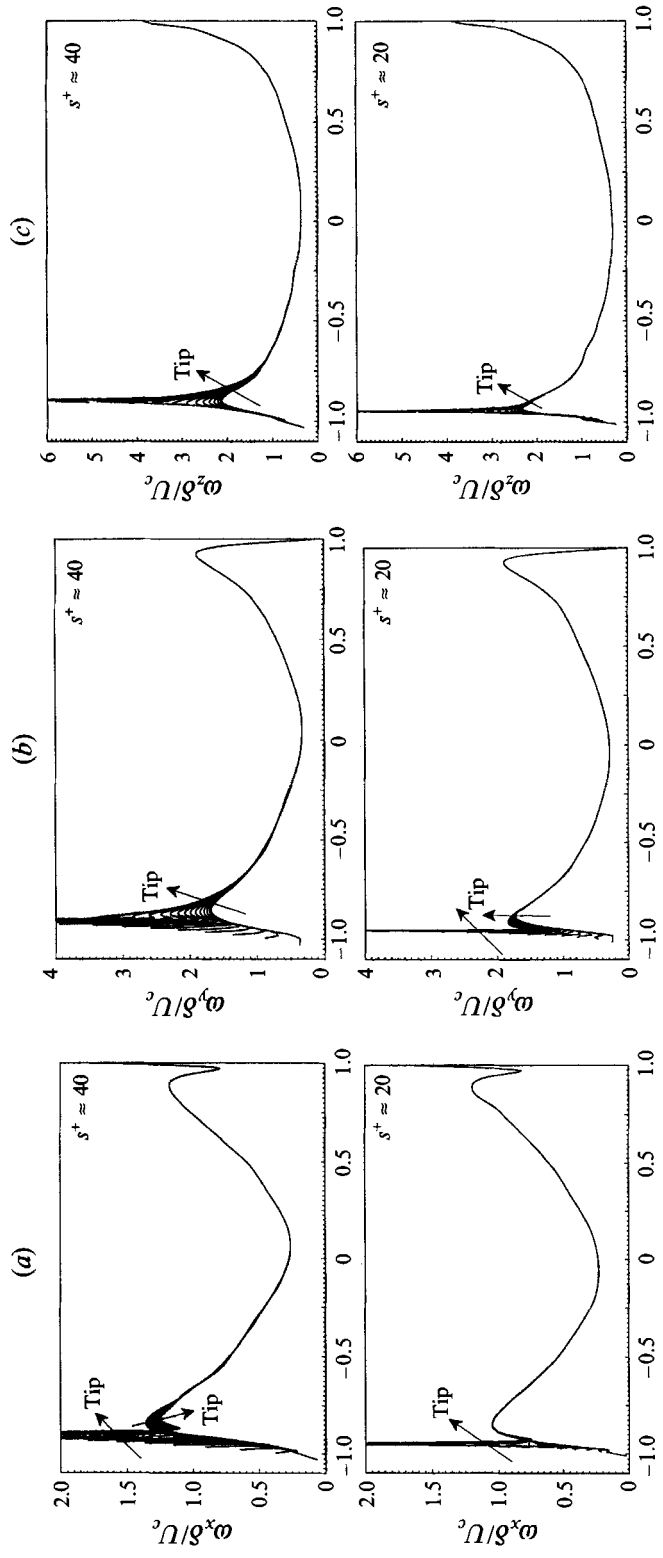

FIGURE 16. Root-mean-square vorticity fluctuations normalized by the mean centreline velocity U_c and channel half-width δ in global coordinates for $\alpha = 60°$. (*a*) Streamwise; (*b*) normal; (*c*) spanwise vorticity fluctuations.

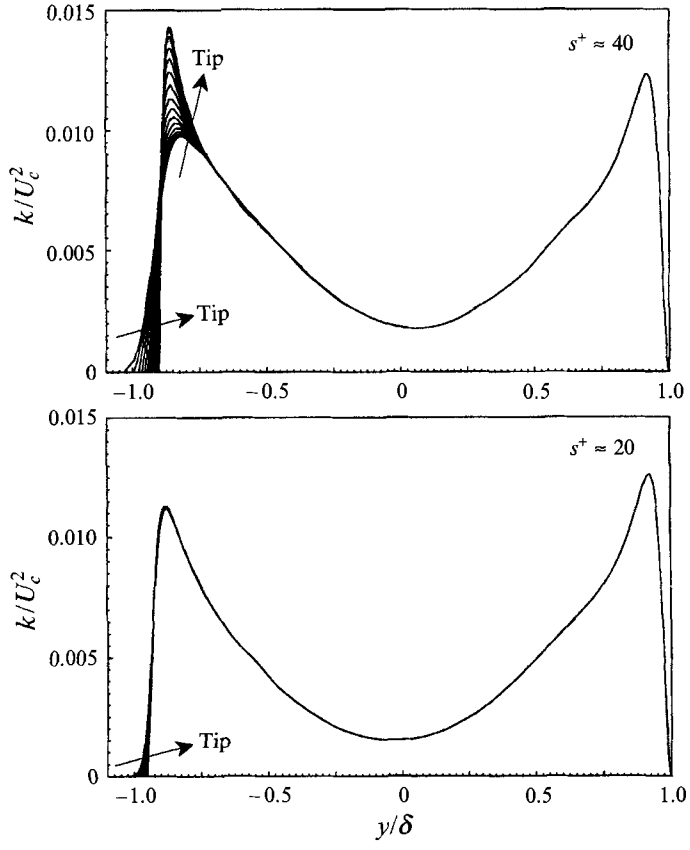

FIGURE 18. Turbulent kinetic energy normalized by the mean centreline velocity U_c for $\alpha = 60°$. $k = \frac{1}{2}(\overline{u'^2}+\overline{v'^2}+\overline{w'^2})$.

y from all four quadrants is the mean Reynolds shear stress at y. For all cases considered, the ejection event is dominant away from the wall, and the sweep event has larger contributions in the wall region. Regardless of the riblet spacing and lateral position about the riblet, the Reynolds shear stresses from the first- and third-quadrant events are nearly unchanged except for a small outward shift of the data. The maximum values from the first- and third-quadrant events are $-\overline{u'v'}/U_c^2 \approx -0.0005$ for all cases considered here (figure 20*a*, *b*). However, the Reynolds shear stresses from the second- and fourth-quadrant events are changed by the riblets. In the case $s^+ \approx 40$, the maximum value of the Reynolds shear stress from the ejection (second-quadrant) event is reduced above the riblet valley but is substantially increased above the riblet tip. The Reynolds shear stress from the sweep (fourth-quadrant) event is also significantly reduced very near the riblet valley but increased very near the riblet tip. However, there is no noticeable difference in the fourth-quadrant event above $y/\delta \approx -0.7$ (figure 20*a*).

In the case $s^+ \approx 20$, there is virtually no spanwise variation of the Reynolds shear stress except very near the riblets. Hence, the profiles above the three different spanwise locations show essentially the same result except very near the riblets. The maximum values of the Reynolds shear stress from the second- and fourth-quadrant events are reduced, while those from the first- and third-quadrant events are almost unchanged

fluctuations occur only very near the riblets in the case $s^+ \approx 20$, while in the case $s^+ \approx 40$ there is further penetration into the channel.

Reductions of all three components of the vorticity fluctuations by the riblets occur in the drag-reducing configuration ($s^+ \approx 20$). The local maximum streamwise vorticity fluctuation above the riblets is reduced by 12% as compared with that above the flat plate. The local maximum of the normal vorticity fluctuation is reduced only marginally. In the case $s^+ \approx 40$, vorticity fluctuations are increased above the riblets. It is interesting to note that, near the local maximum ($y/\delta \approx -0.8$), ω_x above the riblet valley is larger than that above the riblet tip, but the converse is true for ω_y and ω_z.

Root-mean-square vorticity fluctuations normalized by the wall-shear velocity u_τ are shown in figure 17. As described in §§5.1 and 5.2, use of the virtual origin y_o and the wall-shear velocity $u_{\tau_r}^*$ collapses the peak locations as well as the magnitudes of the vorticity fluctuations for the case $s^+ \approx 20$ but not for the case $s^+ \approx 40$. The local maximum ω_x occurs at $y^+ \approx 20$ regardless of the presence of the riblets, which suggests that the centre of the streamwise vortex is located on average at $y^+ \approx 20$ (Kim *et al.* 1987). It is clear from figure 16(*a*) that, in the case $s^+ \approx 20$, the streamwise vortices above the riblets are weakened (compare the peak values near $y/\delta \approx \pm 0.8$).

5.4. *Quadrant analysis*

Quadrant analysis of the Reynolds shear stress provides detailed information on the contributions to the total turbulent energy production from various combinations of positive and negative u' and v' (Willmarth & Lu 1972; Wallace, Eckelmann & Brodkey 1972). The total turbulent energy production P_k is

$$\begin{aligned} P_k &= -\overline{u_i' u_j'} S_{ij} \\ &= -\overline{u'^2}\frac{\partial \overline{u}}{\partial x} - \overline{v'^2}\frac{\partial \overline{v}}{\partial y} - \overline{w'^2}\frac{\partial \overline{w}}{\partial z} \\ &\quad -\overline{u'v'}\left(\frac{\partial \overline{u}}{\partial y}+\frac{\partial \overline{v}}{\partial x}\right) - \overline{u'w'}\left(\frac{\partial \overline{u}}{\partial z}+\frac{\partial \overline{w}}{\partial x}\right) - \overline{v'w'}\left(\frac{\partial \overline{v}}{\partial z}+\frac{\partial \overline{w}}{\partial y}\right), \end{aligned} \tag{14}$$

where S_{ij} is the mean strain-rate tensor. For the present study, $\partial\overline{u}/\partial x = \partial\overline{v}/\partial x = \partial\overline{w}/\partial x = 0$ due to flow homogeneity in the streamwise direction.

Turbulent kinetic energy k and turbulent energy production P_k are shown in figures 18 and 19. Maximum turbulent kinetic energy is reduced by 10% in the case $s^+ \approx 20$, but, in the case $s^+ \approx 40$, it is increased above the riblet tip and is decreased above the riblet valley. The turbulent energy production exhibits the same behaviour as the turbulent kinetic energy. In the case $s^+ \approx 20$, the peak of the turbulent energy production occurs at $y^+ \approx 13$, as mentioned in §4.2. However, in the case $s^+ \approx 40$, the peak location varies slightly. All terms except $-\overline{u'v'}\,\partial\overline{u}/\partial y$ on the right-hand side of (14) are negligible away from the riblets. Very near the riblets these terms are not negligible, but are still an order of magnitude smaller than $-\overline{u'v'}\,\partial\overline{u}/\partial y$.

Since most of the turbulent energy production comes from $-\overline{u'v'}\,\partial\overline{u}/\partial y$, we restrict our quadrant analysis to the Reynolds shear stress $-\overline{u'v'}$. The analysis divides the Reynolds shear stresses into four categories according to the signs of u' and v'. The second ($u' < 0$ and $v' > 0$; ejection) and fourth ($u' > 0$ and $v' < 0$; sweep) quadrant events contribute to positive production, and the first ($u' > 0$ and $v' > 0$) and third ($u' < 0$ and $v' < 0$) quadrant events contribute to negative production.

The contributions to the Reynolds shear stress from each quadrant, normalized by the mean centreline velocity, are shown in figure 20. The sum of the values at a position

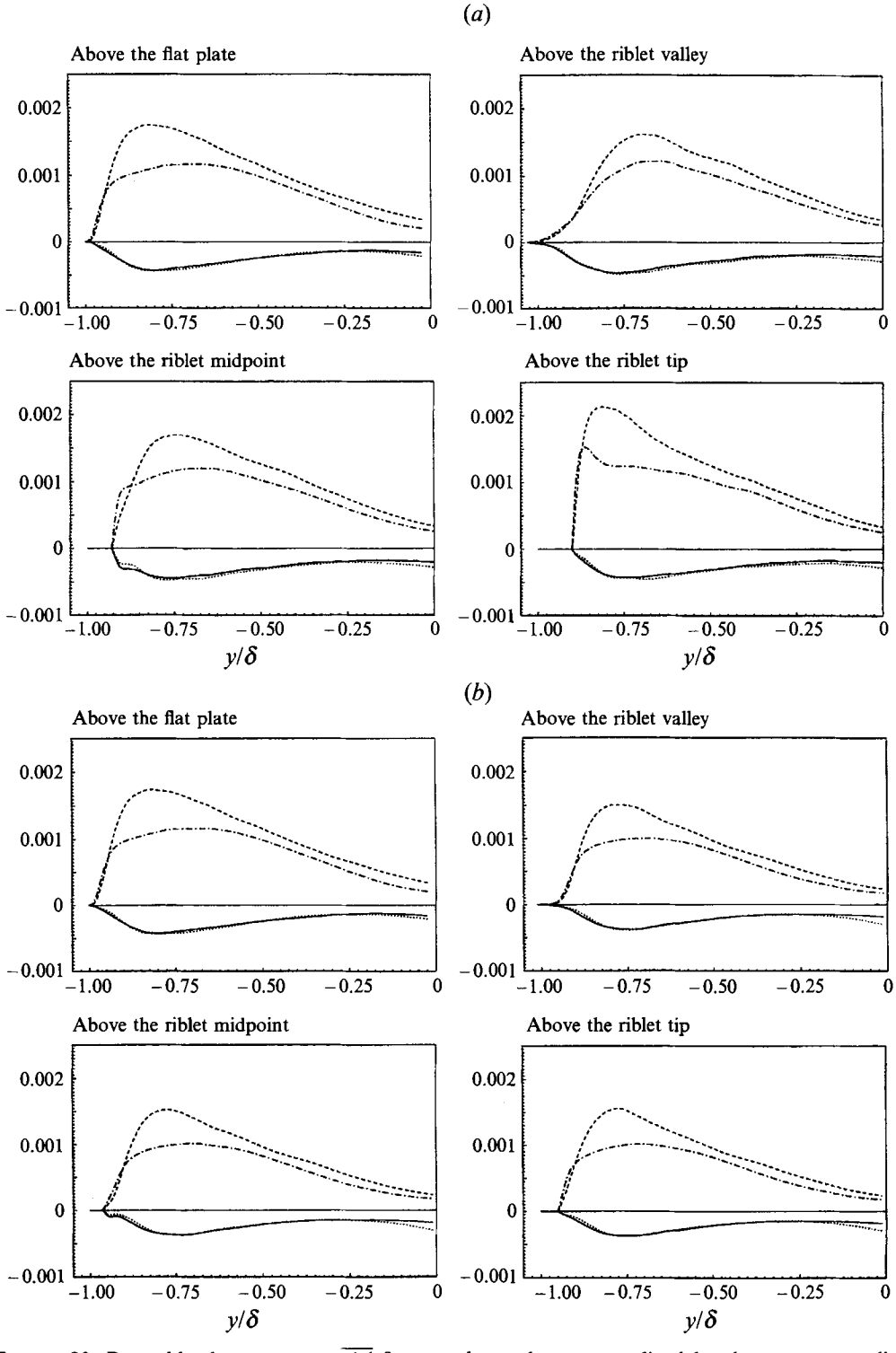

FIGURE 20. Reynolds shear stress $-\overline{u'v'}$ from each quadrant normalized by the mean centreline velocity U_c for $\alpha = 60°$: —, first; – – –, second; · · · · · · · · ·, third; – · –, fourth quadrant. (*a*) $s^+ \approx 40$; (*b*) $s^+ \approx 20$.

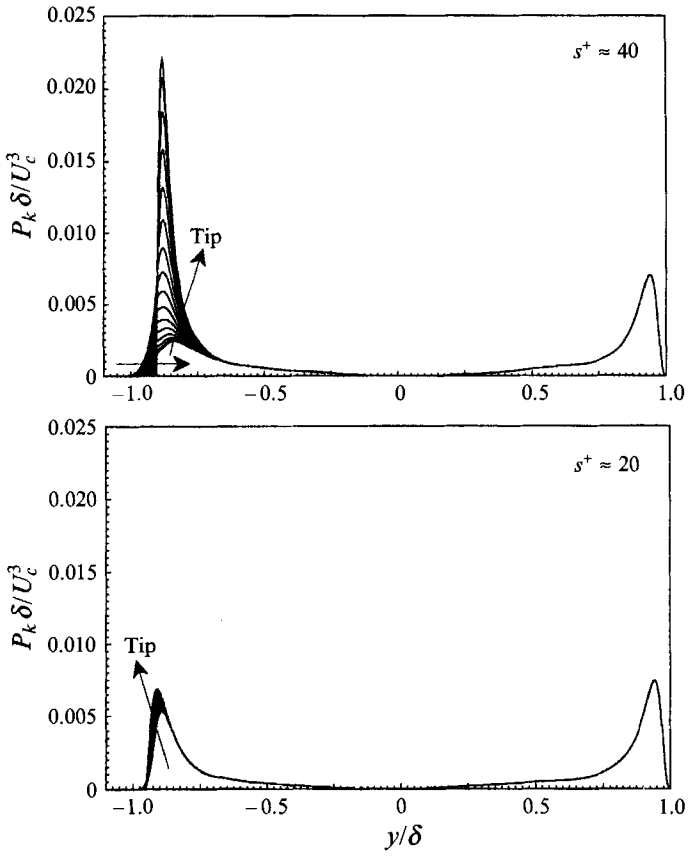

FIGURE 19. Turbulent energy production normalized by the mean centreline velocity U_c and the channel half-width δ for $\alpha = 60°$.

(figure 20*b*), indicating that only the positive Reynolds-shear-stress-producing events are changed by the riblets. Accordingly, the riblets intensify the positive Reynolds-shear-stress-producing events in a drag-increasing configuration, while they mitigate the positive Reynolds-shear-stress-producing events in a drag-reducing configuration.

It is well known that the streamwise vortices in turbulent boundary layers contribute to positive production via the second- and fourth-quadrant events, while the first- and third-quadrant events are not correlated with the streamwise vortices and may be related to background turbulence. Since the riblets modify the positive Reynolds-shear-stress-producing events and do not change the first- and third-quadrant events, it may be deduced that the riblets are most effective in modifying the organized motion associated with the streamwise vortices.

The contribution to the Reynolds shear stress from each quadrant, normalized by the local mean Reynolds shear stress ($-\overline{u'v'}$), is shown in figure 21. This plot shows the fractional contribution from each quadrant event to the local mean Reynolds shear stress. Above the flat plate, the contributions from the ejection and sweep events are about the same at $y^+ \approx 10$. In the case $s^+ \approx 40$, the location at which the contributions from the ejection and sweep events are equal varies. However, in the case $s^+ \approx 20$, this location is fixed at $y^+ \approx 10$. The fractional contribution from each quadrant is nearly the same as that for the flat plate above $y^+ \approx 20$. The sharp increases in the normalized

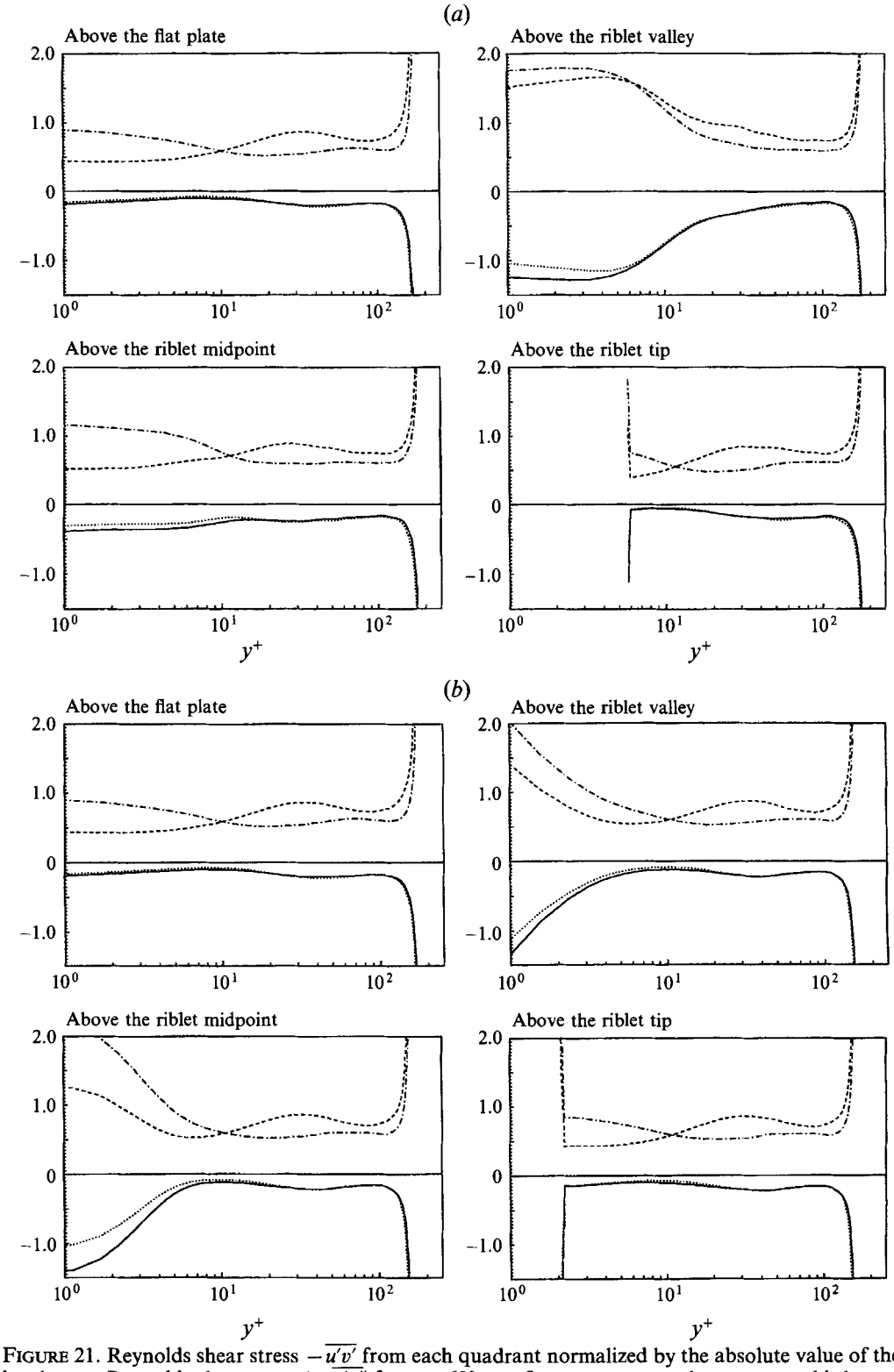

FIGURE 21. Reynolds shear stress $-\overline{u'v'}$ from each quadrant normalized by the absolute value of the local mean Reynolds shear stress $|-\overline{u'v'}|$ for $\alpha = 60°$: —, first; – – –, second; · · · · · · · · ·, third; –·–, fourth quadrant. (*a*) $s^+ \approx 40$; (*b*) $s^+ \approx 20$.

Reynolds shear stress from each quadrant near the riblet tip and the centreline in figure 21 simply reflect the small mean Reynolds shear stress at those locations.

Pulles *et al.* (1989) found from a quadrant analysis at $y^+ \approx 38$ that there was a lower fractional contribution from the second quadrant and a higher contribution from the fourth quadrant above the riblets compared to those above the flat plate, and they concluded that ejections were weaker above the riblet and sweeps were much stronger. However, a higher fractional contribution from fourth-quadrant events does not imply stronger sweep motions above the riblets because the absolute magnitude of the Reynolds shear stress from the fourth-quadrant events above the riblets may still be lower than that above the flat plate. Our results show that this is indeed the case (figures 20 and 21).

5.5. *Higher-order statistics*

The skewness and flatness factors of the velocity fluctuations are shown in figures 22 and 23. The skewness of w' should be zero away from the riblets because of the reflectional symmetry of the flow statistics. The skewness and flatness factors are nearly unchanged above $y^+ \approx 30$, but are significantly changed near the riblets. The skewness of u' is decreased near the riblet valley, while it is increased near the riblet tip. For $10 < y^+ < 15$, in the case $s^+ \approx 40$, the skewness of u' is increased across the entire span. The skewness of v' reaches large negative values near the riblet valley and large positive ones near the riblet tip.

The flatness of u' is decreased very near the riblet valley and increased near the riblet tip. However, the flatness of v' is significantly reduced above both riblet tip and valley, indicating that the normal velocity above the riblets is less intermittent than in the flat-plate case. The flatness of w' is nearly unchanged in the case $s^+ \approx 20$, while it is slightly reduced in the case $s^+ \approx 40$.

Hooshmand *et al.* (1983) and Bacher & Smith (1985) found that riblets have no effect on the skewness of the velocity fluctuations. However, they measured the skewness of u' only for $y^+ > 10$. As is clearly indicated in figures 22(*b*) and 23(*b*), in the case $s^+ \approx 20$ (a drag-reducing configuration), the difference in the skewness and flatness factors occurs only for $y^+ < 10$. Coustols & Cousteix (1989) reported that the skewness and flatness of the streamwise velocity fluctuations were reduced near $y^+ = 5$, while there were no modifications for $y^+ > 20$ ($y^+ = 0$ corresponded to the riblet tip in their data). On the other hand, Tardu & Truong (1991) found that the skewness and flatness of u' were increased for $y^+ < 15$. As shown in figures 22(*b*) and 23(*b*), in the presence of riblets there is a significant spanwise variation of the skewness and flatness of u' below $y^+ \approx 10$. Hence, the spanwise locations of their measurements should have been indicated to clarify this issue. Vukoslavčević *et al.* (1992) reported that the skewness and flatness of u' near the riblets significantly increase above the riblet valley and decrease above the riblet tip, which apparently contradicts the present results. However, this discrepancy is due to the fact that each of their profiles was vertically shifted to match the origin of the flat wall. When replotted with the same coordinates used here, the same conclusion is drawn: i.e. at a given y^+ (< 10), the skewness and flatness of u' are increased above the riblet tip and decreased above the riblet valley. However, the present data do not show such large skewness and flatness factors very near the riblet valley as in Vukoslavčević *et al.* (1992).

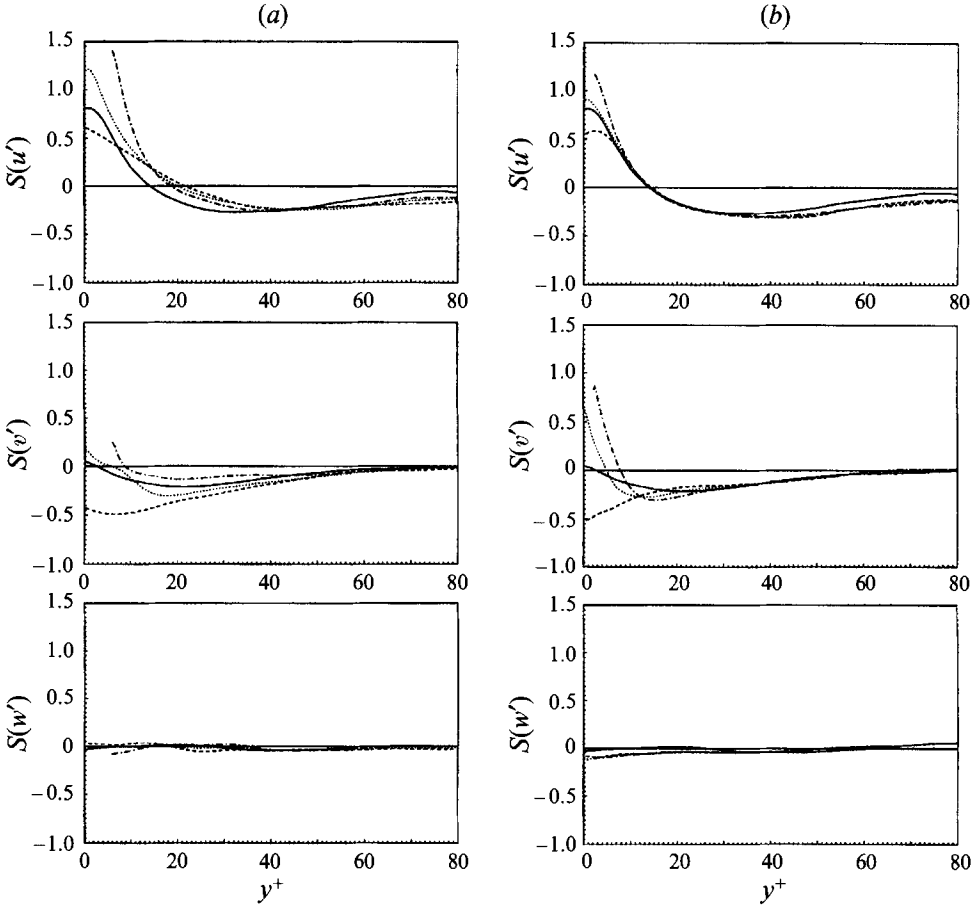

FIGURE 22. Skewness factors in wall coordinates: —, above the flat plate; – – –, above the riblet valley; · · · · · · · · ·, above the riblet midpoint; –·–, above the riblet tip. (*a*) $s^+ \approx 40$; (*b*) $s^+ \approx 20$. $y^+ = (y - y_o)\, u_{\tau_r}^*/\nu$.

5.6. *Further comparison with experimental results*

Detailed comparison of turbulence statistics above riblets is difficult among the existing data in the literature. There are differences in the riblet shapes and sizes as well as Reynolds numbers and the proximity of the measurement locations to the riblets. Surprisingly, there are also several experimental studies of the flow characteristics near riblets that do not include drag measurements. Some measurements that do include turbulence statistics do not report the spanwise location of the measurements. To the authors' knowledge, the experiments of Benhalilou *et al.* (1991) and Vukoslavčević *et al.* (1992) are the only available measurements that report on the spanwise variation of turbulence statistics near riblets. Their Reynolds numbers, Re_τ, were about 160 and 470, respectively, which are in the range of the present study. The same riblet geometry, $\alpha = 45°$ (i.e. $s^+ = 2h^+$), was used in both experiments. The non-dimensional riblet spacing was reported to be $s^+ \approx 30$ in Benhalilou *et al.* (1991) and 35 in Vukoslavčević *et al.* (1992). Unfortunately, neither study provided skin-friction data.

The root-mean-square streamwise velocity fluctuations of Benhalilou *et al.* (1991) and Vukoslavčević *et al.* (1992) are replotted in figure 24 together with the present data. As in the experimental data, for comparison, the profiles above the tips and valleys

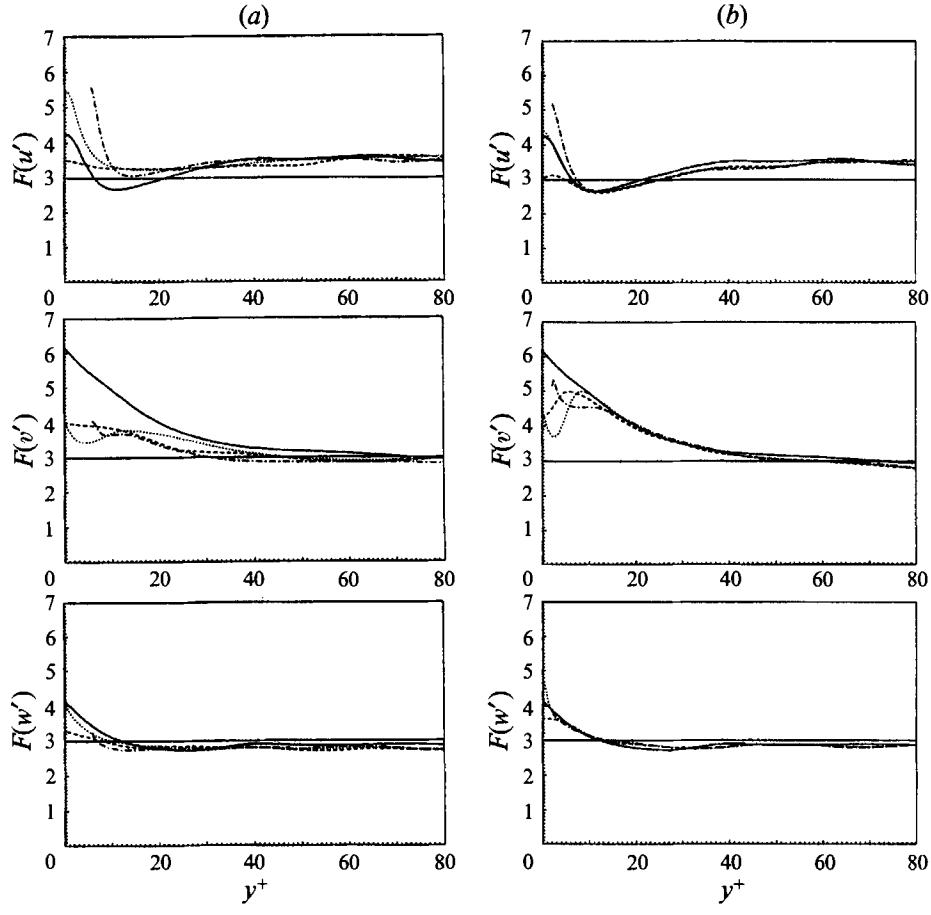

FIGURE 23. Flatness factors in wall coordinates: —, above the flat plate; – – –, above the riblet valley; · · · · · · · · ·, above the riblet midpoint; –·–, above the riblet tip. (*a*) $s^+ \approx 40$; (*b*) $s^+ \approx 20$. $y^+ = (y - y_o)u^*_{\tau_r}/\nu$.

were shifted vertically so that their origins would coincide with the location of a reference flat plate located halfway between a tip and valley ($y/\delta = 0$). There is an apparent trend in the u' profiles: regardless of riblet spacing, the y-locations of the maximum turbulence intensity above the riblet tips are closer to the origin ($y/\delta = 0$) than that above the corresponding flat plate, whereas the peak y-locations above the riblet valleys are further away from the origin. Reductions or increases of the root-mean-square streamwise velocity fluctuations above the riblet valley and tip were discussed in §5.1 and will not be repeated here. As shown in figure 24, the data by Benhalilou *et al.* (1991) and Vukoslavčević *et al.* (1992) are similar to the present results for $s^+ \approx 40$ and $s^+ \approx 20$, respectively. We also plotted all the experimental and computational turbulence intensities in the wall coordinates (u'/u_{τ_f} *vs.* y^+), where y^+ has been obtained by using the virtual origin of Bechert & Bartenwerfer (1989). However, these data did not collapse well. This is probably due to different riblet spacings as well as measurement difficulties very near the riblets.

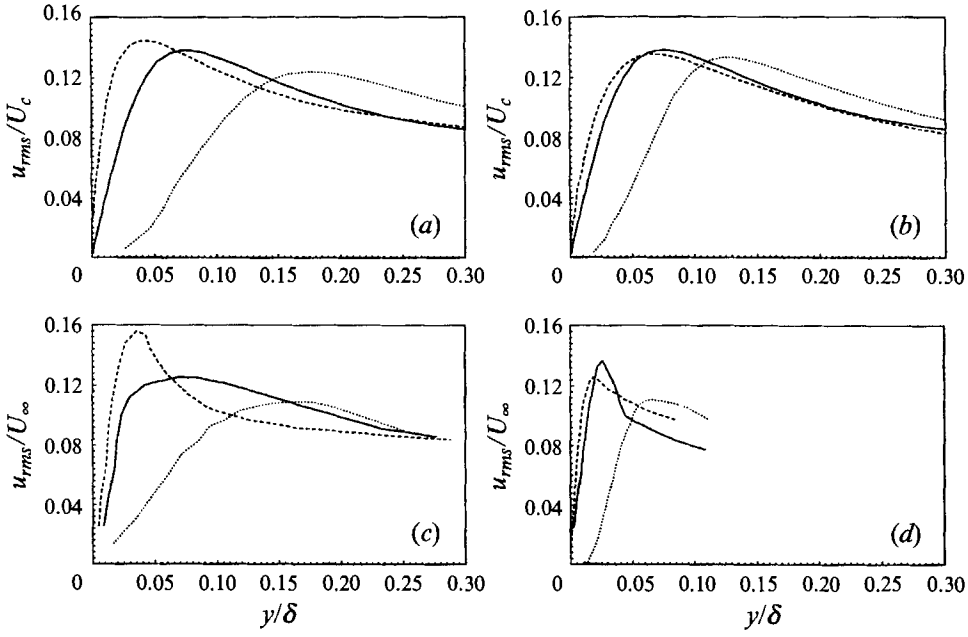

FIGURE 24. Profiles of the streamwise velocity fluctuation intensity above the riblet with $\alpha = 45°$ in global coordinates: —, above the flat plate; – – –, above the riblet tip; · · · · · · · · ·, above the riblet valley. (*a*) From the present data ($s^+ \approx 40$); (*b*) from the present data ($s^+ \approx 20$); (*c*) from Benhalilou *et al.* (1991) ($s^+ \approx 30$); (*d*) from Vukoslavčević *et al.* (1992) ($s^+ \approx 35$). Note that the profiles over the tips and valleys are shifted vertically so that the surfaces of the riblet valleys and tips have the same vertical coordinate origin ($y/\delta = 0$) as the smooth flat plate.

6. Drag reduction mechanism

As mentioned in § 5, in the case $s^+ \approx 20$, there was a decrease of the Reynolds stresses near the riblets, suggesting that riblets reduce momentum transport by impeding the cross-flow motion. The strengths of the streamwise vortices above the riblets are also reduced (figure 16*a*), indicating that the downwash and ejection motions due to the streamwise vortices are weakened.

In this section, we focus on the time-dependent turbulence structures above riblets by examining the instantaneous flow fields. Our objective is to elucidate the physical mechanism by which riblets reduce drag.

Figure 25(*a*) (plate 1) shows contours of the instantaneous wall-shear rate $\partial u/\partial n$ normalized by U_l and δ on the riblet surfaces for cases with $\alpha = 60°$. The non-dimensionalized plane- and time-averaged wall-shear rate on the flat plate is 7.8, and the wetted area of the plate with riblets is sec (α) times greater than that of the flat plate. Hence, a wall-shear rate on the riblet surface that is larger than $7.8\cos(\alpha)$ results in an increased drag on the riblet surface over that of the flat plate, whereas a value smaller than $7.8\cos(\alpha)$ results in a decrease. The black lines in figure 25(*a*) show the contour line with value $7.8\cos(\alpha)$. Regions of high wall-shear rate (red contours) can be seen not only near the riblet tips but also in the middle of the riblets in the case $s^+ \approx 40$, whereas in the case $s^+ \approx 20$ the regions of high wall-shear rates are restricted to the tips.

It has been shown in Choi *et al.* (1992) that, in plane channel flow, local regions of high skin friction are associated with streamwise vortices just above the wall. The sweep motion due to these strong streamwise vortices creates regions of high skin

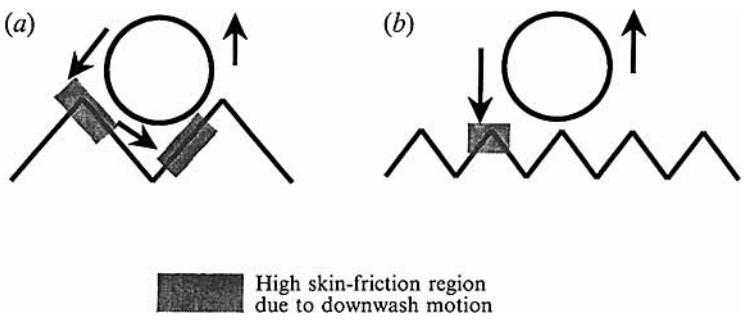

FIGURE 26. Schematic diagram of drag increase and reduction mechanisms by riblets: (*a*) $s^+ \approx 40$ – drag increase (extensive area affected by downwash motion); (*b*) $s^+ \approx 20$ – drag reduction (limited area affected by downwash motion).

friction on the wall. The transverse-flow structures leading to high skin friction can be seen in the cross-sectional views at the locations (marked with arrows in figure 25*a*) at which the highest wall-shear rates occur. Figure 25(*b*) shows cross-flow velocity vectors (v, w) and contours of the streamwise vorticity component in the transverse plane. Strong streamwise vortices near the riblets are present in both cases. It was estimated in Kim *et al.* (1987) from the profile of root-mean-square streamwise vorticity in plane channel flow that the centres of streamwise vortices are located on average at $y^+ \approx 20$, and that their average diameter is $d^+ \approx 30$. Since the average diameter of the streamwise vortices above the wall is smaller than the spacing of the riblets in the case $s^+ \approx 40$, the streamwise vortices can move freely and can be found inside the riblet valleys. This exposes a larger surface area of the riblets to the sweep motion that they induce. On the other hand, in the case $s^+ \approx 20$, most streamwise vortices stay above the riblets because their average diameter is larger than the spacing of the riblets, and only a limited area of the riblet tips is exposed to their induced sweep. A schematic diagram of this drag modification mechanism is shown in figure 26. Note that even in the case of riblets with $s^+ \approx 40$ the skin friction per unit of surface area is reduced due to less, but still significant, inhibition of streamwise vortices approaching the wetted area. In the case $s^+ \approx 20$, only a small part of the wetted surface is exposed, resulting in a net drag reduction despite a significant increase in the wetted area.

Several other instantaneous flow fields were examined, and in none of the cases with $s^+ \approx 20$ were strong streamwise vortices observed in between the riblets. On the other hand, each instantaneous flow field in the case $s^+ \approx 40$ contained streamwise vortices between the riblets. The wall-shear rate profiles in figure 6(*a*) clearly support the proposed mechanism: the wall shear rate in the case $s^+ \approx 40$ is noticeably higher than that in the case $s^+ \approx 20$ in the middle of the riblet surface, whereas the wall shear rates near the tip and valley regions are nearly identical.

Of course there is a distribution of the diameters of the near-wall streamwise vortices. At present this distribution has not been deduced from measurements or simulation data. Such a distribution would be very valuable for a more quantitative analysis of drag reduction by riblets. Our proposed mechanism for drag reduction by riblets implicitly assumes that the typical diameter of the dynamically significant streamwise vortices is around 30 wall units.

7. Summary

Direct numerical simulations of turbulent flows over riblets were carried out at a

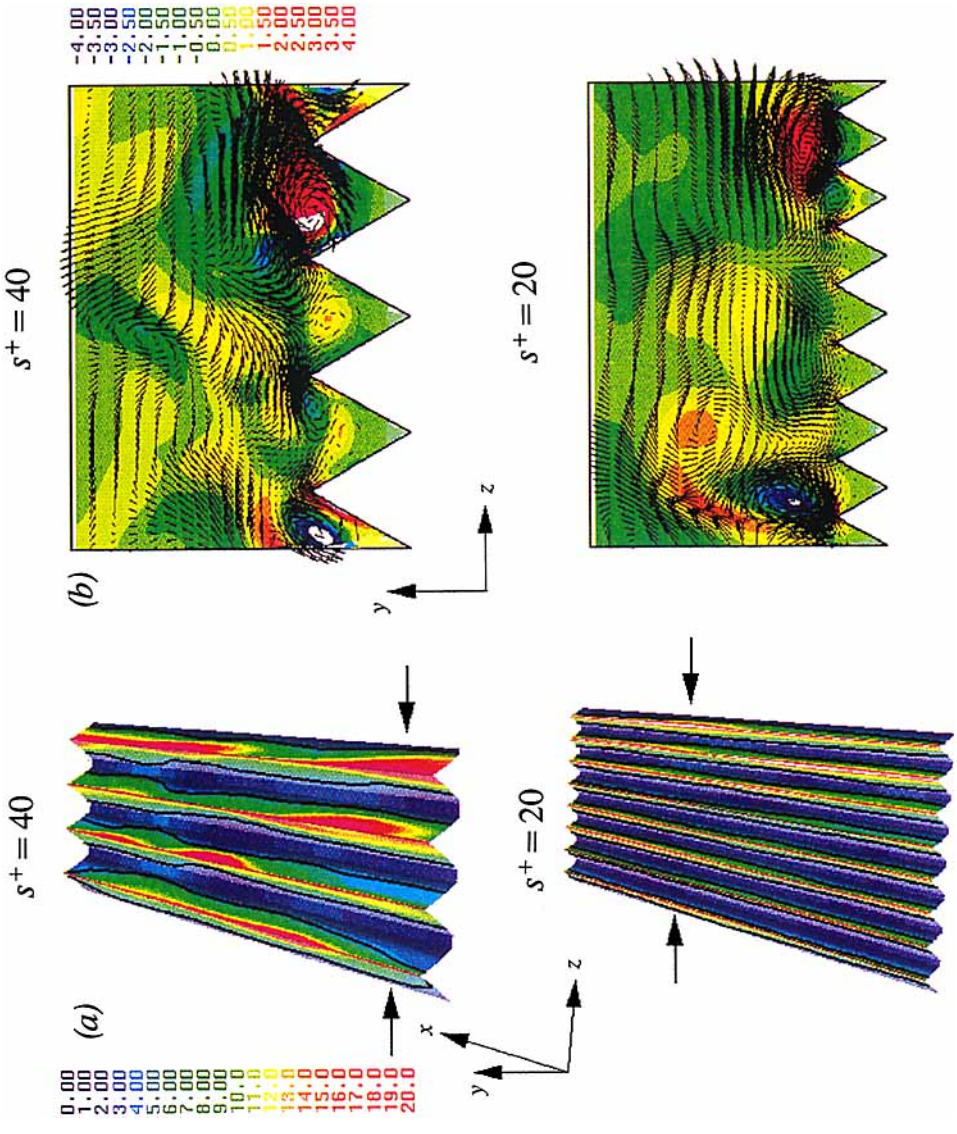

FIGURE 25. Instantaneous flows over the riblets with $\alpha = 60°$: *(a)* contours of the wall-shear rate on the riblet surfaces; *(b)* cross-flow velocity vectors (v, w) and contours of the streamwise vorticity in the (y, z)-plane.

Reynolds number of 4200 based on the centreline velocity of a laminar parabolic profile (with the same volume flux) and the channel half-width. A fully implicit (Crank–Nicolson) fractional step method was used for the time-advancement, and a second-order central finite-difference method was used for the spatial derivatives.

The drags computed for each riblet configuration were in good agreement with the experimental results of Walsh (1982). Cases with $s^+ \approx 20$ showed a 5–6% drag reduction, and cases with $s^+ \approx 40$ showed a drag increase.

The virtual origin of the wall was defined such that the maximum turbulent kinetic energy production occurred at $y^+ \approx 13$. As the ridge angle of the riblets increased, the virtual origin moved closer to the riblet tip. The mean-velocity profiles based on these virtual origins showed upward and downward shifts in the log–law for drag-decreasing and drag-increasing cases, respectively.

Flow statistics above the riblets were compared to those above the flat plate. Differences between the mean-velocity profiles and turbulence quantities were limited to the inner region of the boundary layer. Velocity and vorticity fluctuations as well as the Reynolds shear stress above the riblets were reduced in drag-reducing configurations. Reduction of the normal and spanwise velocity fluctuations above the riblets indicated that the transverse flow near the wall was impeded by the riblets, one of the drag reduction 'mechanisms' suggested by Bechert & Bartenwerfer (1989) and Choi (1989). Quadrant analysis indicated that the riblets intensified the positive Reynolds-shear-stress-producing events in drag-increasing configurations, while they mitigated these (second- and fourth-quadrant) events in drag-reducing configurations. The Reynolds shear stresses from the first- and third-quadrant events were nearly unchanged by the riblets, implying that the riblets modify only the organized motion that is associated with the streamwise vortices above the wall.

From an examination of the instantaneous flow fields, a drag reduction mechanism was proposed: a certain spacing of riblets reduces viscous drag by restricting the location of streamwise vortices above the wetted surface such that only a limited area of the riblets is exposed to the downwash of high-speed fluid induced by them. Only the tip region is exposed to high wall-shear rates in drag-reducing configurations, whereas in drag-increasing configurations both the middle and tip regions are exposed to them.

Note added in proof. While this paper was being printed, a paper by Chu & Karniadakis on the flow over riblets appeared in this Journal (*J. Fluid Mech.* vol 250 (1993), p. 1). Although some of their flow statistics above the riblets are in general agreement with the present data, there are noticeable discrepancies between the two computations. In particular, they report instantaneous flow reversals near riblet valleys where the magnitude of flow reversal reached as high as 2.5% of the bulk streamwise velocity. This is not in accordance with the present computations. Examination of forty of our instantaneous flow fields revealed only a handful of isolated grid points where the streamwise velocity was slightly negative (less than 0.1% of the centreline velocity). Such negative values are within the error bounds of the iterative solvers used and cannot be attributed to physical effects.

Support from the Air Force Office of Scientific Research under Contract No. AFOSR-89-0411 is gratefully acknowledged. The computer program used in this study was developed in cooperation with Professor Paolo Orlandi. His contributions are greatly appreciated. We also thank Dr Robert Rogallo and Mr Thomas Bewley for useful comments on a draft of the manuscript.

REFERENCES

BACHER, E. V. & SMITH, C. R. 1985 A combined visualization-anemometry study of the turbulent drag reducing mechanisms of triangular micro-groove surface modifications. *AIAA Paper* 85-0548.

BANDYOPADHYAY, P. R. 1986 Review – Mean flow in turbulent boundary layers disturbed to alter skin friction. *Trans. ASME* I: *J. Fluids Engng* **108**, 127.

BECHERT, D. W. & BARTENWERFER, M. 1989 The viscous flow on surfaces with longitudinal ribs. *J. Fluid Mech.* **206**, 105.

BENHALILOU, M., ANSELMET, F., LIANDRAT, J. & FULACHIER, L. 1991 Experimental and numerical investigation of a turbulent boundary layer over riblets. In *Proc. 8th Symp. on Turbulent Shear Flows, 9–11 September 1991, Technical University of Munich*, pp. 18.5.1–18.5.6.

BUSHNELL, D. M. & MCGINLEY, C. B. 1989 Turbulence control in wall flows. *Ann. Rev. Fluid Mech.* **21**, 1.

CANTWELL, B. J. 1981 Organized motion in turbulent flow. *Ann. Rev. Fluid Mech.* **13**, 457.

CHOI, H., MOIN, P. & KIM, J. 1991 On the effect of riblets in fully developed laminar channel flows. *Phys. Fluids* A **3**, 1892.

CHOI, H., MOIN, P. & KIM, J. 1992 Turbulent drag reduction: studies of feedback control and flow over riblets. *Rep.* TF-55. Department of Mechanical Engineering, Stanford University, Stanford, CA.

CHOI, K.-S. 1989 Near-wall structure of a turbulent boundary layer with riblets. *J. Fluid Mech.* **208**, 417.

COUSTOLS, E. & COUSTEIX, J. 1989 Experimental manipulation of turbulent boundary layers in zero pressure gradient flows through external and internal devices. In *Proc. 7th Symp. on Turbulent Shear Flows, 21–23 August 1989, Stanford University, California*, pp. 25.3.1–25.3.6.

COUSTOLS, E. & SAVILL, A. M. 1992 Turbulent skin-friction drag reduction by active and passive means. In *Special Course on Skin Friction Drag Reduction* (ed. J. Cousteix), *AGARD Rep.* 786.

GALLAGHER, J. A. & THOMAS, A. S. W. 1984 Turbulent boundary layer characteristics over streamwise grooves. *AIAA Paper* 84-2185.

GAUDET, L. 1987 An assessment of the drag reduction properties of riblets and the penalties of off-design conditions. *RAE TM* 2113.

HOOSHMAND, A., YOUNGS, R. A., WALLACE, J. M. & BALINT, J.-L. 1983 An experimental study of changes in the structure of a turbulent boundary layer due to surface geometry changes. *AIAA Paper* 83-0230.

JIMÉNEZ, J. & MOIN, P. 1991 The minimal flow unit in near-wall turbulence. *J. Fluid Mech.* **225**, 213.

JOHANSEN, J. B. & SMITH, C. R. 1986 The effects of cylindrical surface modifications on turbulent boundary layers. *AIAA J.* **24**, 1081.

KIM, J., MOIN, P. & MOSER, R. 1987 Turbulence statistics in fully developed channel flow at low Reynolds number. *J. Fluid Mech.* **177**, 133.

LAUNDER, B. E. & LI, S. 1989 A numerical study of riblet effects on laminar flow through a plane channel. *Appl. Sci. Res.* **46**, 271.

LIU, K. N., CHRISTODOULOU, C., RICCIUS, O. & JOSEPH, D. D. 1990 Drag reduction in pipes lined with riblets. *AIAA J.* **28**, 1697.

LUCHINI, P., MANZO, F. & POZZI, A. 1991 Resistance of a grooved surface to parallel flow and cross-flow. *J. Fluid Mech.* **228**, 87.

LUMLEY, J. L. 1973 Drag reduction in turbulent flow by polymer additives. *J. Polymer Sci.* D: *Macromol. Rev.* **7**, 263.

MOFFATT, H. K. & DUFFY, B. R. 1980 Local similarity solutions and their limitations. *J. Fluid Mech.* **96**, 299.

NAKAO, S.-I. 1991 Application of V shape riblets to pipe flows. *Trans. ASME* I: *J. Fluids Engng* **113**, 587.

NGUYEN, V. D., SAVILL, A. M. & WESTPHAL, R. V. 1987 Skin friction measurements following manipulation of a turbulent boundary layer. *AIAA J.* **25**, 498.

NIKURADSE, J. 1930 Turbulente Strömung in nichtkreisförmigen Rohren. *Ing.-Arch.* **1**, 306.

NIKURADSE, J. 1933 Stromungsgesetze in rauher rohen. *VDI-Forschungsheft* 361. (Also, Laws of flow in rough pipes. *NACA TM* 1292).

NITSCHKE, P. 1984 Experimental investigation of the turbulent flow in smooth and longitudinal grooved tubes. *NASA TM* 77480.

PULLES, C. J. A., PRASAD, K. K. & NIEUWSTADT, F. T. M. 1989 Turbulence measurements over longitudinal micro-grooved surfaces. *Appl. Sci. Res.* **46**, 197.

ROBINSON, S. K. 1988 Effects of riblets on turbulence in a supersonic boundary layer. *AIAA Paper* 88-2526.

ROBINSON, S. K. 1991 Coherent motions in the turbulent boundary layer. *Ann. Rev. Fluid Mech.* **23**, 601.

ROGALLO, R. S. & MOIN, P. 1984 Numerical simulation of turbulent flows. *Ann. Rev. Fluid Mech.* **16**, 99.

ROSENFELD, M., KWAK, D. & VINOKUR, M. 1991 A fractional step solution method for the unsteady incompressible Navier–Stokes equations in generalized coordinate systems. *J. Comput. Phys.* **94**, 102.

SAWYER, W. G. & WINTER, K. G. 1987 An investigation of the effect on turbulent skin friction of surfaces with streamwise grooves. *RAE TM* 2112.

SCHLICHTING, H. 1936 Experimentelle untersuchungen zum rauhigkeits problem. *Ingenieur-Archiv VII* **1**, 1. (Also, Experimental investigation of the problem of surface roughness. *NACA TM* 823).

TANI, I. 1988 Drag reduction by riblet viewed as roughness problem. *Proc. Japan Acad.* B **64**, 21.

TARDU, S. & TRUONG, T. V. 1991 In *Proc. 6th European Drag Reduction Meeting, August 1991, Eindhoven.*

VIRK, P. S. 1975 Drag reduction fundamentals. *AIChE J.* **21**, 625.

VUKOSLAVČEVIĆ, P., WALLACE, J. M. & BALINT, J.-L. 1992 Viscous drag reduction using streamwise-aligned riblets. *AIAA J.* **30**, 1119.

WALLACE, J. M. & BALINT, J.-L. 1987 Viscous drag reduction using streamwise aligned riblets: survey and new results. In *Turbulence Management and Relaminarisation* (ed. H. W. Liepman & R. Narasimha). Springer.

WALLACE, J. M., ECKELMANN, H. & BRODKEY, R. S. 1972 The wall region in turbulent shear flow. *J. Fluid Mech.* **54**, 39.

WALSH, M. J. 1980 Drag characteristics of V-groove and transverse curvature riblets. In *Viscous Drag Reduction* (ed. G. R. Hough). AIAA.

WALSH, M. J. 1982 Turbulent boundary layer drag reduction using riblets. *AIAA Paper* 82-0169.

WALSH, M. J. 1983 Riblets as a viscous drag reduction technique. *AIAA J.* **21**, 485.

WALSH, M. J. & WEINSTEIN, L. M. 1978 Drag and heat transfer on surfaces with small longitudinal fins. *AIAA Paper* 78-1161.

WILKINSON, S. P. & LAZOS, B. S. 1987 Direct drag and hot-wire measurements on thin-element riblet arrays. In *Turbulence Management and Relaminarisation* (ed. H. W. Liepman & R. Narasimha). Springer.

WILLMARTH, W. W. & LU, S. S. 1972 Structure of the Reynolds stress near the wall. *J. Fluid Mech.* **55**, 65.